Towards the development of a three-dimensional, human induced pluripotent stem cell-based tauopathy model for spatial and temporal analysis of pathology

By

Rachel Boone

Thesis

Submitted to the Faculty of the

Graduate School of Vanderbilt University

in partial fulfillment of the requirements

for the degree of

MASTER OF SCIENCE

in

Chemical Engineering

August 31, 2021

Nashville, Tennessee

Approved:

Ethan S. Lippmann, Ph.D.

Scott A. Guelcher, Ph.D.

A very special thanks to my family whom I dedicate this work to for believing in me

and

To my incredibly supportive boyfriend for encouraging me not to give up in challenging times

and

Last but certainly not least, my most loyal companion Hazel

ACKNOWLEDGEMENTS

I would like to acknowledge and express sincere gratitude to Professor Ethan Lippmann for his support in my research efforts. His patient guidance and direction has helped me develop and practice valuable research and professional skills that I will carry on into the future. I respect and admire his dedication to this field and achievements he has made throughout his young career. I am impressed by the vast scope and ability the lab has to offer and I am extremely grateful for the time I had to work and learn under his leadership.

I would like to thank several members of the Lippmann Lab for training me and helping me learn techniques. A special thanks to Ketaki Katdare for her generosity and support in providing cells in critical time which allowed many of these experiments to be possible. To many members who helped train me on various techniques or helped run experiments including Lexi Yates, Madison Stiefbold, Kylie Balotin, Allison Bosworth, Yajuan Shi, Everett Allchin and Alex Sorets. A special thanks to Sarah Sturgeon for always being very kind and helpful in offering her time to explain and teach me concepts so that I can become a better scientist.

A very special thanks to Dr. Brian O' Grady, a post-doctoral fellow in the Lippmann group for all his guidance and support in helping in many aspects from preparing 3D prints, setting up and running diffusion experiments, and suggesting solutions to overcome challenges as they arose and beyond in offering assistance and advice. Your dedication, expertise and ingenuity have helped me indefinitely. I am extremely grateful for your assistance and hard work that developed these materials and protocols making much of this work possible. I look forward to seeing his accomplishments as he continues to excel in research and his academic career.

Finally, I acknowledge my financial support from National Science Foundation Graduate Research Fellowship Program Base Award No. 1937963.

This material is based upon work supported by the National Science Foundation Graduate Research Fellowship Program under Grant No. 1937963. Any opinions, findings, and conclusions or recommendations expressed in this material are those of the author(s) and do not necessarily reflect the views of the National Science Foundation.

TABLE OF CONTENTS

LIST OF TABLES

LIST OF FIGURES

Chapter 1

Introduction

1.1 Motivation

In recent decades, an aging population prevalence has highlighted the need for addressing neurodegenerative diseases and their causes; yet, no cure exists for such disorders and treatment options are primarily limited to symptomatic relief[1]. Neurological diseases are among the most challenging to study in part due to difficulty in obtaining human brain tissue in early stages of disease and lack of appropriate human or animals models to accurately mimic pathophysiology[2]. Consistent failure of pharmaceuticals to provide therapeutic benefit and low success rate of new therapies in Phase 1 trials reinforces the need for more physiologically relevant models to investigate underlying disease mechanisms and provide more accurate predictions in pre-clinical testing[3].

1.2 Tauopathies and prion-like pathogenesis

Despite their differences in etiology, most neurodegenerative diseases share common features including the progressive spread of protein abnormalities accompanied by neuroinflammation and neural dysfunction[4]. Tauopathies are a group of progressive neurodegenerative diseases characterized by the presence of hyperphosphorylated, misfolded varieties of tau protein encoded by the microtubule-associated protein tau (MAPT) gene[5]. In healthy brains, tau is expressed in the central nervous system (CNS) to promote and help stabilize microtubule assembly as well as facilitate axonal transport[6]. All six isoforms native to the adult human brain contain either three or four repeat units collectively referred to as the repeat domain (RD) region flanked by a proline-rich region which contribute strongly to microtubule binding and assembly[7]. More specifically, three isoforms contain all four microtubule binding repeats (consisting of 31-32 amino acids each) and three lack the second repeat (R2) or exon 10; they also differ in whether they contain two, one or no amino terminal inserts in its projection domain (N of 29

amino acids) summarized in Figure 1[8]. These variations allow the protein to naturally vary in size from 352 to 441 amino acids long in the adult brain due to alternative mRNA splicing[8,9]. In humans, various mutations in the repeat or microtubule binding domain (MTBD) region, especially those involving exon 10 such as ΔK280, P301L[9], P301S MAPT mutants, or exon 11 such as S320F[10], have been heavily researched in cell culture studies due to their propensity to induce efficient tau aggregation[11] and strong connection to early-onset familial and parkinsonism frontotemporal dementia (FTD) phenotypes[12–14].

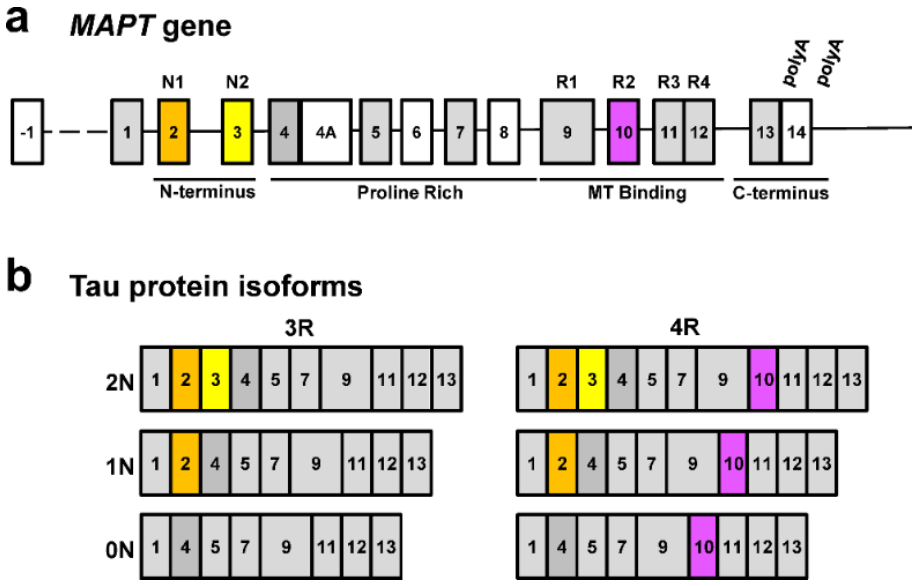

Figure 1: Alternative splicing of MAPT mRNA transcripts results in six isoforms of the gene which include the MTBD and a proline rich region[8]. The constitutive exons are shown in grey, alternate coloring highlights sites affected by alternative splicing and colorless represent exons not transcribed in the human CNS.

While genetic contributions have been identified, the vast majority of tauopathies occur sporadically. Nonetheless, these genetic risk factors provide key insight to underlying protein irregularities that contribute to pathophysiology. For example, it is established that specific mutations and post-translational modifications, especially hyperphosphorylation, in the microtubule binding repeats (or MTBD) of tau remove the region's positive charge and affinity to negatively charged microtubules. Consequently, this may trigger a pathological cascade depicted in Figure 2[15] whereby unfolded, highly soluble monomers combine into pathological oligomers, eventually forming insoluble, intracellular aggregates known as neurofibrillary tangles (NFTs). Normal tau contains about 2-3 moles of phosphate per mole of protein,

while tau in Alzheimer's disease may contain up to 3-4-fold more phosphorylated sites, and these highly-phosphorylated forms are the major protein component in forming paired helical filaments (PHFs) and NFTs[16]. Tau mutations such as the P301L variant differ from wild-type by a single amino acid, yet are known to significantly accelerate formation of PHFs and enhance β-sheet propensity for aggregate formation[17]. Their spatiotemporal pattern of accumulation or distinct deposition trajectories correlate with clinical progression and disease severity[16,18].

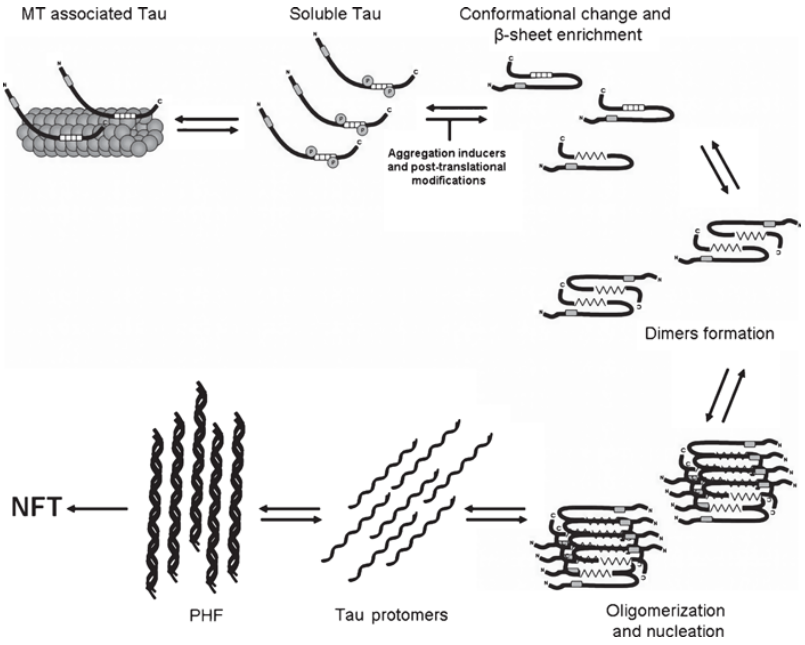

Figure 2: Aberrant hyperphosphorylation or other aggregation inducing modifications of tau result in destabilization and disassembly form microtubules, leading to conformational changes to aggregation competent forms. Destabilization of microtubule binding promotes polymerization to ultimately adopt dense, β-sheet rich structures typical of amyloid aggregates[15].

The many factors that may influence tau aggregation, multiple confirmations involved, and diverse mechanisms of possible secretion and uptake give rise to the heterogeneity observed in progression of tau-mediated pathology[19]. No single neurotoxic form is recognized, and it is unlikely an explicit confirmation is responsible for the progressive neuronal loss and resultant cognitive decline. Regardless, increasing accumulation of hyperphosphorylated and filamentous tau in neurons and glia in afflicted brain regions are hallmark features observed in AD and similar tauopathies, which correlates with advanced spread

between brain areas during the clinical course[20]. While the molecular basis and mechanisms of action behind tau-induced neurodegeneration are not fully defined, it is confirmed that increased phosphorylation of tau and formation of NFTs are strongly associated with the disruption in normal physiological function and this phenomenon must be further investigated to elucidate tau function and dysfunction.

Emerging evidence suggests tau pathology may progress via trans-cellular propagation whereby the protein exhibits "prion-like" seeding behavior[21]. According to this theory, soluble or oligomer forms of abnormal tau referred to as 'seeds' are secreted and may be subsequently taken up by neighboring cells through a variety of endocytosis pathways as shown below in Figure 3[22–24]. Neuronal internalization mechanisms are diverse, non-exclusive and sometimes include: clathrin-mediated, heparan sulfate proteoglycan and caveolae-mediated pathways to name a few of interest depending on the species[22,25]. Ultimately, the spread of exogenous tau seeds induces seeded aggregation and filament growth. This occurs as seeds promote protein misfolding via templated self-assembly by recruiting endogenous tau monomers for addition leading to further aggregation and progression of pathology as depicted in Figure 3[23]. Thus, the challenge of modeling tau propagation is to capture certain aspects of spread in space and time which emphasizes the utility of engineering more adaptable, physiologically relevant three-dimensional (3D) platforms useful to all facets or research.

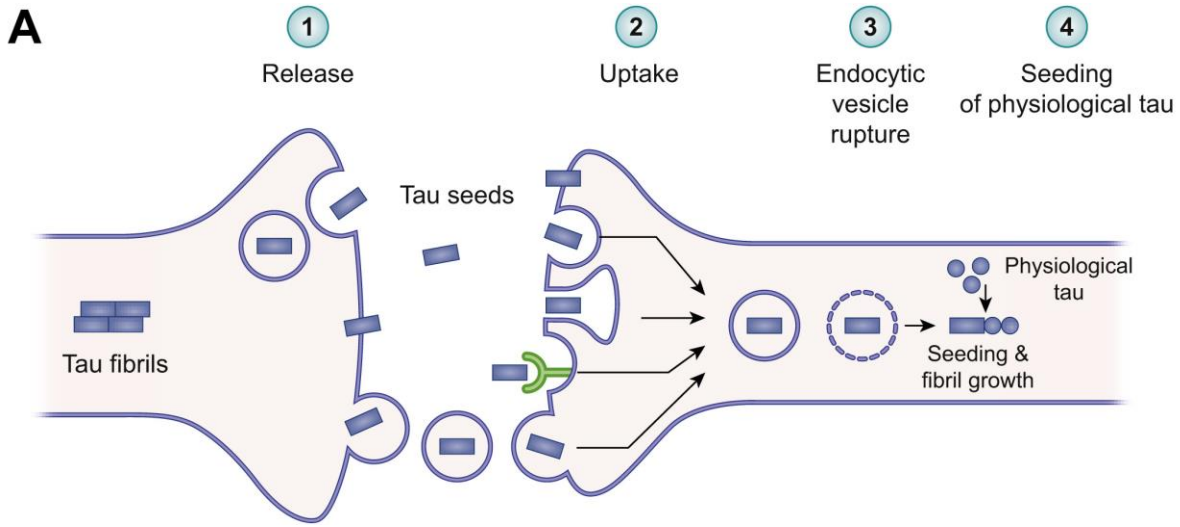

Figure 3: Conceptual depiction of methods of intercellular tau propagation which occur after pathologic tau seeds are released and taken up via a variety of mechanisms to a neighboring neuron(s). Internalized tau seeds may act as templates for additional growth of tau aggregates and fibrils[24].

1.3 Three-dimensional human-based models and simulation to investigate propagation

Human based *in vitro* neuronal models have provided valuable tools for studying neurodegenerative diseases[26]. Of various cell culture options, human induced pluripotent stem cell (iPSC)-derived neural cultures have grown increasingly popular for modeling neurological disease phenotypes and drug screening[27]. In addition to avoiding issues of species translatability[26], iPSC cultures offer high expansion efficiency due to their unlimited self-renewal and capability of being differentiated into any cell type under appropriate culture conditions[28]. Human cortical cultures of glutamatergic neurons derived from iPSCs were the cell choice for this model as deleterious changes and dysfunction in the excitatory glutamatergic system is heavily implicated in cognitive impairment and pathogenesis of several tauopathies including AD, the most prevalent neurodegenerative disorder[29–31]. Biomaterials and microfluidic devices have enhanced cultures by allowing more sophisticated, biomimetic 3D systems to more closely mimic characteristics of tissue and the brain's extracellular matrix (ECM) without requiring large material quantities[32]. These are valuable in disease model development, as traditional 2D cultures lack the structural complexity of native tissue or supportive function of the ECM, therefore these artificial conditions are incapable of reproducing all pathological events leading to neurodegeneration[26].

In this regard, 3D tissue engineered neural constructs offer vast improvements- biocompatible and bioactive properties of hydrogel scaffolds and other matrices better reproduce *in vivo* intercellular and matrix interactions provided by the ECM. Furthermore, 3D microfluidic platforms are often capable of more precise fluid manipulation and permit intercellular communication via diffusion and interstitial flow. The patterning abilities of fluidic technologies enables control of cell microenvironment and morphology, and systems developed using iPSC-derived brain organoids or neural cultures report encouraging evidence for researching CNS diseases and more specifically neurodegenerative disorders[27,33]. Microfluidics developed using inert 3D prints as molds or stencils to cast PDMS devices is a recent strategy that permits fabrication of more complex, modular systems for biological research with microchannels mounted to a glass substrate for convenient imaging[34–36]. A key objective of 3D *in vitro* cell models is to recapitulate naturally occurring signaling cues, protein gradients, etc. which result from secretion and diffusion of biomolecules; thus the common dual-chamber barrier module separated by a central chamber for addition of seeded scaffold or other separate reservoirs/chamber chip designs are useful to study effects of small molecule gradients[37].

Finally, when forming and studying dynamic chemical gradients, it is imperative to be able to predict and understand the external driving forces and transport phenomenon. In many cases, it is useful to create a finite element model (FEM) using software such as COMSOL Multiphysics® to compute concentration profiles for prototyping and to adapt the system as desired. To inform the physical model used in this work, we used COMSOL Multiphysics® as supplement for efficient calculation and prediction of complex transport/behavior of tau protein in a 3D cellular microenvironment. Together, the components previewed above were combined in the initial steps towards development of a fully-defined, customizable 3D neural network for analyzing spatiotemporal effects of tau seeding activity, with preliminary findings to form the basis for more specific future studies.

Chapter 2

Materials and Methods

2.1 | Cell culture

CC3 iPSCs were maintained in E8 medium[38] on 6-well tissue culture plates coated with growth-factor reduced Matrigel (Corning™ 354234) to support cell attachment and expansion[38,39]. Cells were passaged upon reaching 60-80% confluence using Versene solution (Thermo Fisher 15040) first by washing and then incubating for 5 minutes at 37°C[40]. The process for deriving cortical glutamatergic neurons from iPSCs is adapted from the procedure described by Shi et al. (2012)[41,42]. This is a simplified and widely used differentiation protocol for producing functional neural networks from human iPSCs with a near 100% efficiency of induction of cortical neural fate[41,42]. After washing confluent iPSCs with PBS (Invitrogen 14190144) cells were isolated using Accutase (Thermo Fisher A1110501) by incubating for 3 minutes. Cells were then pelleted via centrifugation and seeded according to the live cell density obtained using a Countess™ II (Thermo Fisher) onto 12-well Matrigel coated plates at $2x10^5$ cells/cm^2 in E8 medium containing 10 μM Y27632 (Rho-associated kinase ROCK inhibitor, Tocris 12-541-0). On the following day after checking for ~100% confluency, the 12 day neural induction period was initiated by switching medium to E6 supplemented with small molecule signaling pathway inhibitors LDN 193189 and SB 431542 (0.4 μM and 10 μM, Tocris 60-531-0 and 16-141-0) for 5 days[43]. Media was gradually transitioned to N2 Medium (DMEM/F12 basal medium, Gibco 11330-032) containing 1X N2 supplement (Gibco 17502048) replenishing the concentrations of small molecule inhibitors with daily media change[41–43]. On day 11 of differentiation, neural progenitors were isolated by 1 hour of Accutase incubation and replated into 12-well Matrigel coated plates in a Neural Maintenance Medium of equal volume N2 Medium and B27 Medium (Neurobasal Medium, Gibco 21103049 supplemented with 200 mM Glutamax, Gibco 35050-061) and 1X B27 (Stem Cell Technologies 05711) containing 10 μM Y27632 at a cell density of $1x10^5$ cells/cm^2. Over the subsequent 20-day neural stem cell expansion and differentiation period Neural Maintenance Medium (neuron media) was replaced daily and every 3-4 days thereafter.

Neurons were cultured for up to 100 days with experiments performed beginning at maturity on differentiation day 70.

2.2| Microfluidic device fabrication

A 3D-printed mold designed in Autodesk Fusion 360 (Autodesk, San Rafael, CA, US) was printed with a Form 3 printer (Formlabs, Somerville, MA, USA) using black or clear resin. Parylene C coating was vapor deposited on the print using a SCS Labcoter® 2 Parylene Deposition System (Specialty Coating Systems, KISCO) to protect the integrity to endure multiple uses and prevent cytotoxic residues from leaching from the print. Polydimethylsiloxane (PDMS) base was formed using a PDMS kit by mixing the Silicone Elastomer Base and Curing Agent (Sylgard 184, Dow Silicones Corporation, #02065622) in a 9:1 elastomer base to curing agent ratio. Once poured over top of the parylene coated print, the PDMS mixture was degassed for 30 minutes to remove bubbles. After heating at 80 °C for at least 30 minutes, the print was carefully removed ensuring pillars remained intact and 6 ports made at the tops and bottoms of both reservoirs and central chamber using a 1.5 mm biopsy punch (Miltext Ted Pella, 15119-1). The open PDMS surface was then thoroughly cleaned to remove dust. A large cover glass with 0.16-0.18mm thickness (Ted Pella, 260461-100) was also cleaned and both PDMS mold and glass slide were treated in an expanded plasma cleaner (Harrick Plasma, 230V PDC-002) for at least 15 minutes to remove organic contaminants and activate the PDMS surface. This enables mounting of the cover glass by forming an irreversible seal between the glass and PDMS[44]. The fabricated microdevices were autoclaved for sterile use in sealed sterilization pouches (Fisher, FSC-01-812-54) on wrapped setting (Heidolph Tuttnauer 3870, Tuttnauer USA, Hauppague, NY).

2.3| Synthesis of biomaterial scaffold

The following summarizes the 2-step process used to synthesize Redox-Cad gel. A 4.2% solution of Gelatin from porcine skin (300 g Bloom, Sigma G1890) is stirred in PBS at 50°C until dissolved, and pH is adjusted to 5-6 using 1M HCl. Gelatin is conjugated to a custom N-cadherin peptide epitope containing a reactive C-terminal carboxyl (C(=O)OH-HAVDIGGGC, produced through GenScript). Exposed primary amines on the gelatin structure enable conjugation to the custom epitope (1:125 g peptide:gelatin)

via a 2-step coupling reaction using 1-Ethyl-3-(3-dimethylaminopropyl)carbodiimide (1:125 g EDC:gelatin, Thermo Fisher 77149) and N-Hydroxysuccinimide (1:83.33 g NHS:gelatin, Thermo Fisher 24500), to achieve carboxyl-to-amine crosslinking. The conjugation solution containing EDC, NHS and N-cadherin is dissolved separately in PBS with DMF (10.42% original reaction volume, 3:2 PBS:DMF) and allowed 30 minutes to react before adding dropwise to react for 2.5 hours at 37°C.

Reaction step two involves HPA conjugation, initiated by dissolving HPA (1:125 g HPA:gelatin) in the same solvent mixture of EDC and NHS (identical chemical weights and solvent ratios as described for the conjugation solution above) allowed to react for at least 1 hour before dropwise addition. The second reaction completes in 5 hours and functionalizes the hydrogel with redox-crosslinking capability. Both conjugation reactions were carefully timed during synthesis as they compete for the same bonding chemistry on the gelatin backbone. Finally, after adjusting the pH to 8-9 using 5M NaOH, purification was performed by Tangential Flow Filtration (TFF) with 4× volume addition of prewarmed Millipore Milli-Q water (Merck, Darmstadt, Germany) for at least 4 hours replenishing the filter volume regularly. The hydrogel solution, referred to as Redox-Cad is gradually cooled to -80°C and then lyophilized (Labconco 700401000) until dry.

2.4| Characterization and seeding of Redox-Cad hydrogels

After drying, ^{1}H-NMR was conducted on a Bruker DRX 500 Hz NMR spectrometer at 37 °C to confirm the aromatic phenol (HPA) and valine peaks from N-cadherin were present in the gel. Synthesized Redox-Cad gel should contain key peaks around 2.5-2.8 ppm suggesting presence of valine residues which are not present in gelatin. Peaks at 7ppm are indicative of the aromatic hydrogens on HPA and peaks at 2.5-3 ppm are from two acrylic (2H) bonded to the carbons in-between the carboxylic acid and aromatic ring. Peaks corresponding to both structures suggest successful conjugation of both HPA and most importantly N-cadherin. The ^{1}H-NMR spectrum of unmodified gelatin base can be found in the Appendix.

Redox-Cad seeding solutions were prepared in a slightly modified procedure described by O'Grady et al. used for single-cell suspensions of iPSC-derived neurons in the bio-functionally similar material GelMA-Cad[42]. A 10% hydrogel solution in Neurobasal Medium was prepared and bath sonicated at 37 °C for 15 minutes to degas. Post differentiation day 70 iPSC-derived neurons were isolated by lifting from 12-well plates using Accutase (~5-15-minute incubation as necessary to dissociate) and centrifugation. Cells were

reconstituted at 2 × 10^5 cells/mL gel solution. A 10% solution of microbial transglutaminase (mTG, ModernistPantry Moo Gloo TI Transglutaminase) in UltraPure™ Distilled Water (Invitrogen™ 10977023) was added to initiate enzymatic crosslinking of the solution (1.5:100 mTG initiator to hydrogel solution) and mixtures were added to the central chamber of a microfluidic device. Gels in microdevices were added to a petri dish and incubated (37°C and 5% CO_2) until crosslinked or overnight, after which neuron media with 1% Penicillin-Streptomycin Solution 100x (Corning®, 30-002-CI) was added to completely fill both reservoirs. Media was changed every 3-4 days or after each cell viability assay or imaging experiment.

2.5| Porosity and quantification of gel morphology

Crosslinked hydrogel samples were prepared as previously described and swollen hydrogels were cut with a razor blade to section and frozen at -80 °C overnight before lyophilizing until dry. Total porosity was estimated using a variation of the Archimedes/gravimetric method reported by Song et al. 2017[45] using the following equation[45]:

$$\%\ \text{Porosity}\ (\varepsilon_p) = (W_2 - W_3 - W_{\text{dry}})/(W_1 - W_{\text{dry}}) \times 100\% \quad (1)$$

Where W_1 is the weight measurement of the 10 mL centrifuge tube filled with UltraPure water, W_2 is the quality of the centrifuge tube and immersed hydrogel, W_3 is the remaining mass after removing the hydrated sample, and W_{dry} is the dry mass. Samples were saturated by hydrating in UltraPure water prewarmed to 37°C and briefly placed under vacuum to ensure no air bubbles were present and voids were filled to fully hydrate pores. At least three separate samples were prepared for this measurement.

Empty hydrogel or cell-laden samples 14 days post-embedding were prepared similarly for scanning electron microscopy (SEM) to further characterize the porosity and structure of the hydrogel: instead of vacuum treating, the gels were allowed to hydrate at 37°C for 24 hours before sectioning, freezing and lyophilizing. Samples were prepared for image collection by gold coating using a Sputter Coater 108 (Cressington, England) and imaged using a MERLIN SEM with a GEMINI II column (Zeiss Microscopy, Munich, Germany). ImageJ software was used to evaluate the surface porosity, and this value compared to physically measured volumetric quantity. Images were processed in ImageJ by adjusting the threshold

to visually segment pores and quantified using the Analyze Particles function to obtain total pore area and percentage of the surface area.

2.6| Microfluidic diffusion experiments with fluorescently modified tau monomer

Full-length (2N4R) recombinant P301L variant tau (tau^{P301L} rPeptide, T-1014-1) was labeled for confocal imaging experiments with Cyanine-5 or 3 NHS ester (Lumiprobe, 12020/ abcam, ab146452). The dyes were dissolved in organic, anhydrous DMF according to the general protocol provided by Lumiprobe for NHS ester labeling of amino groups[46]. The dye was added at 8 times molar excess of protein suspended in 0.1M sodium bicarbonate buffer (pH 8.2) for a volume ratio 9:1 buffer to dye solution. The mixture was vortexed and continuously agitated for 4 hours. The conjugate was purified by filtering through Sephadex® G-25 Medium using a PD-10 desalting column filtration system following the manufacturer's instructions (Cytivia, GE 17-0851-01). Labeling efficiency was assessed using a NanoQuant Plate™ reader (Tecan) by comparing the reported Cy5 or Cy3 molar concentration to known protein amount used which was determined to be 3.8 ± 0.5 (approximately 3-4 Cyanine labels per tau protein) which is comparable to similarly labeled Cy3 and Cy5-labeled tau monomers[47].

The conjugated tau^{P301L} in PBS solution was added to neuron media at 300 nM (or equivalent PBS volume for control conditions), to one microdevice reservoir while the opposite was filled with pure PBS or neuron media for acellular or cellular experiments, respectively. The change in fluorescent intensity throughout the gel as conjugated tau^{P301L} diffused across the gel/liquid interface for 3 hours was captured using a LSM 710 with incubation chamber by imaging a small section between the center pillars in 5-minute intervals. Neuron media was replenished in both reservoirs immediately at the conclusion of the diffusion experiment and changed every 3-4 days thereafter.

A region of interest (ROI) point was defined and mean fluorescent intensity evaluated using ImageJ software at known distance from the gel/liquid interface (defined as x = 0). Raw data of mean fluorescent intensity across Z-axis time-lapse stacks were processed to extract concentration from this profile (Figure 4). The data were processed by subtracting average intensity of background region measured before conjugated tau^{P301L} was diffused, then normalized to the initial average intensity (at t = 0 sec) within the charged reservoir. Relative values were linearly related to concentration by multiplication factor given the

known initial concentration and maximum signal of the reservoir. Concentration demonstrated expected asymptotic behavior as diffusion progressed, and the trailing end was neglected as needed for subsequent calculations to correct for bleaching effects due to prolonged laser exposure.

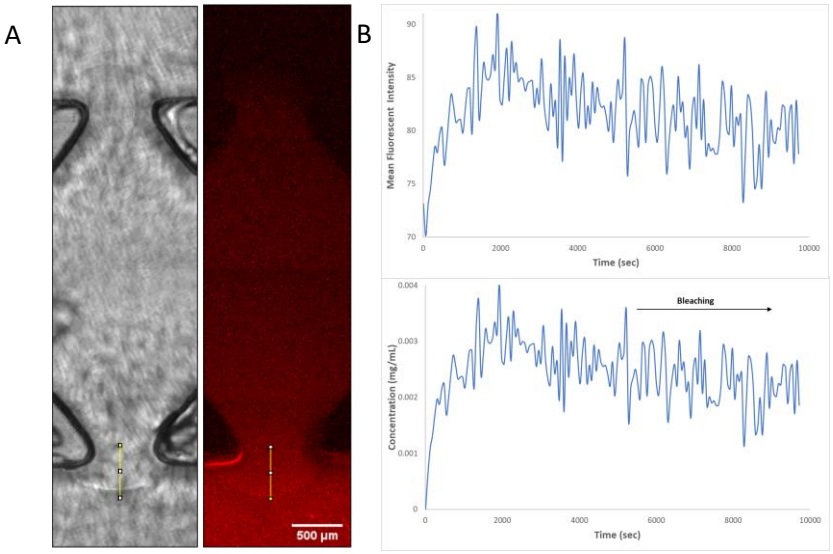

Figure 4: Diffusion coefficient of fluorescently labeled tau (2N4R) with P301L mutation. (Left) Tile scan confocal image capturing the full distance between media reservoirs at an intermediate depth in the gel prior to experiment and after charging the bottom reservoir with Cy5/Cy3 conjugated tau^{P301L} and imaging for 3 hours. (Right) Mean fluorescent intensity and concentration correlation with time measured at a point x = 500 µm from the gel interface.

2.7| Mathematical modeling for estimation of transport parameters

To describe transient diffusion in the porous medium mathematically, the general mass balance equation for transport of diluted species in porous media, generally defined for fully saturated flow (air or media occupies all pores of the gel) is below[48]:

$$\frac{\partial}{\partial t}\left(\varepsilon_p C_i\right) + \frac{\partial}{\partial t}\left(\rho C_{P,i}\right) + \frac{\partial}{\partial t}\left(\theta C_{G,i}\right) + u \cdot \nabla C_i = \nabla \cdot \left[\left(D_{D,i} + D_{e,i}\right)\nabla C_i\right] + R_i + S_i \qquad (2)$$

To simplify, a single phase may be assumed (no solid adsorption or gas volatilization) therefore the second and third terms on the right-hand side of the equation are neglected. Since the fluid is initially charged and not pumped through the system, we may neglect advection (the fourth term = 0 assuming no convection due to velocity flow). These assumptions are valid since fluid transport is driven purely by simple/passive diffusion. On the right-hand side, we may neglect both reaction R_i and source/sink S_i terms for this domain. Finally, assuming no spread occurs due to mechanical mixing and negligible dispersion ($D_{D,i}$ tensor = 0)

this leaves only the effectivity diffusivity term D_e on the right-hand side which is assumed constant and measured experimentally as described above. The simplified result for 1-directional mass transfer of a single species is:

$$\frac{\partial}{\partial t}(\varepsilon_p C) = D_e \frac{\partial^2}{\partial x^2} \quad (3)$$

The porosity ε_p from Equation 3 above is an important coefficient used to balance the mass transport throughout porous medium[48]. Estimation of this parameter was discussed in Section 2.5. Assuming constant surface concentration permits a simple solution to Fick's 2nd law, in summary the following initial and boundary conditions apply:

- For t = 0, $C = C_0$
- For t > 0, $C = C_s$ at x = 0 (gel/liquid reservoir interface is maintained at C_0)
- For t > 0, $C = C_0$ at x = ∞

The concentration dependence of conjugated tau^{P301L} in semi-infinite media can be described using the equation below[49]:

$$C = C_0 \, erfc\left\{\frac{x}{2\sqrt{D_e t}}\right\} + B \quad (4)$$

The adjusted concentration data (mg/mL) collected from images as described above were loaded in Python and compared to values obtained using equation (4) with inputs time (sec) and constants x = 0.05 cm or known distance, initial concentration C_0, to iteratively solve for optimal diffusion coefficient. From at least three independent experiments with fluorescently conjugated tau^{P301L}, the effective diffusion coefficient ($D_e = 1.69 \pm 0.45 \times 10^{-8}$ cm^2/sec) was calculated by minimizing the sum of mean squared errors between calculated concentrations and experiment measurements. An unrelated coefficient B was added as a correction factor for each dataset to improve the fit by correcting for error from imperfect background subtraction. An example of the fit on a concentration dataset is included in the Appendix.

2.8| COMSOL Multiphysics for model prediction

These measured transport properties described were used as inputs in developing a simulation to characterize and predict diffusion behavior in cell-laden gels. Diffusion of fluorescently labeled tau^{P301L} monomer in the microdevice was modeled using the Chemical Reaction Engineering Module in COMSOL Multiphysics® release 5.2a modeling suite (COMSOL AB, Stockholm, Sweden[50]). The Model Wizard was used to construct a 3D, time dependent study using Transport of Diluted Species in Porous Media physics from the Chemical Species Transport Interface. The PDMS microdevice design was modeled in Fusion 360 and exported as a .dxf file from Autodesk Fusion360. Prior to import the geometric design was modified by applying the Fillet operation to remove sharp edges which are not critical to the overall diffusion around pillars within the channel. This helps ensure minimum element sizes would be within range to prevent consequential errors when the minimum size becomes too small for the finite element analysis (FEM) solver to converge. This reasonable approximation of the geometry beneficially reduces computational cost while still giving accurate predictions.

The file was imported and split along the outer edges of the central chamber to partition left and right reservoirs into domains, and a work-plane defined laterally through the device origin to split symmetrically to further simplify computation demand. The left domain was defined as liquid water predefined in the COMSOL materials library database. This selection is reasonable as the primary component of neuron media is DMEM /F12 of which reported densities at 37°C are very similar to water (ρ~0.99g/cm^3) and PBS at this temperature[51]. The dynamic viscosity of water (η) at 37°C is around 0.65-0.69 centipoise (cP) which is within an order of magnitude to that reported of PBS (~0.70 cP)[52] and culture media (DMEM without FBS supplement ~0.731 cP)[51] therefore this is also a reasonable approximation. The reservoir charged with protein solution was defined in the same way with the addition of an initial concentration of 300 nM protein (C_0 = 14.29 μg/mL). The time-dependent study was computed on the porous domain defined using Porous Media Transport Properties with the experimentally determined effective diffusion coefficient (D_e) and porosity (ε_p) of the gel. The left and right domains were defined with basic Transport Properties including a reaction term that is further described below.

$$\frac{\partial C_i}{\partial t} + \nabla \cdot [-D_i \nabla C_i] = R_i \quad (5)$$

The diffusion coefficient in the free media was estimated using the Stokes-Einstein relation:

$$D_i = \frac{kT}{6\pi\eta R_H} \quad (6)$$

Where k is the Boltzmann constant (1.380649×10^{-23} J/K), T is the absolute temperature (310.15 K), η is the viscosity of the solution (~0.70 cP) and R is the hydrodynamic radius of the particle which according to literature, tau monomer solution tends to contain stable oligomers with R_H ~ 4.7 nm at 37 °C[53]. With these values the free diffusion coefficient for the media domains was approximated to be 6.9×10^{-7} cm^2/s. Finally, the boundary conditions were defined as no flux across the solid PDMS frame which forms the interface for gel and media, an initial concentration of C = 0 throughout the gel chamber and right reservoir and initial concentration in the left reservoir defined as $C_{0,C} = C_0$. Symmetry boundaries were defined along the middle z and y-axis to mirror geometry across the splits. Free Tetrahedral mesh qualities were confirmed within range (optimal average ~ 1, and no less than 0.1) and calibrated for Fluid dynamics with Normal element size parameters before simulating the 3-hour diffusion[54].

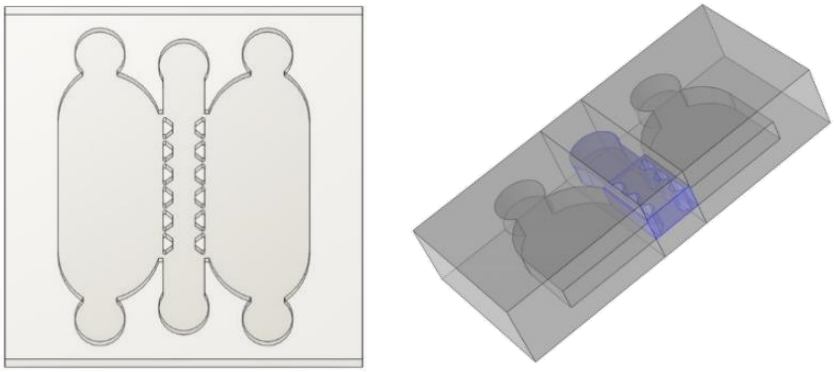

Figure 5: Fusion 360 model of the PDMS microdevice (left) and COMSOL geometry (right) with central domain where the porous media transport study is defined. Final geometry was reduced to necessary components needed for the study and sharp edges filleted to be compatible for finite element analysis (FEM).

To model the second diffusion phase involving removal of the protein source at the conclusion of the diffusion experiment by replacing reservoir contents with fresh media, a time dependent reaction term was implemented to both left and right domains containing a negative reaction rate of -0.01 mol/m^3. A time-delayed pulse was added with a negative reaction rate to approximate the rapid removal of protein solution by pipette. A Gaussian pulse function (gp) is a reasonable approximation for an ultrashort pulse to capture the instants required to remove all protein from both reservoirs by media change while providing a gradual

magnitude and duration without being too rapid to cause numerical instability for the solver. The pulse function was defined in the reaction term of the reservoir domains to achieve a temporal intensity profile (Equation 7):

$$\text{Pulse} * (\text{NegativeRate}) * \left(\frac{t}{1[sec] - Delay}\right) \quad (7)$$

so that the Delay term activates the brief negative reaction once the 3-hour diffusion completes. The negative rate expression was chosen intuitively based on concentration left in the reservoir after the 3-hour diffusion to give the brief pulse sufficient magnitude to remove all protein from both sides.

2.9| Diffusion experiments for validation of simulation results

To validate the COMSOL model a larger, more accessible open top diffusion system was needed to accurately extract concentration from measured distances in the gel for comparison to simulation output. Perfusion in the open-box system developed by O'Grady et al. (2019)[49,55] was the method of choice, with several modifications[49,55]. Instead of cutting two ¼" holes to form parallel channels in the polystyrene box (Ted Pella 139-19) using a mill with plastic cutting drill bit (McMaster-Carr. 27465A84), only 1 channel is needed; therefore, a single hole was drilled using the 3D-printed bioreactor jig as guidance. The polystyrene box was sterilized using repeated bleach and ethanol baths and rinsed in autoclaved water. Autoclaved 1/16-in. silicon tubing (Cole Parmer, cat. No EW-95802-02) was threaded through the holes hosting 3/32" female Luer bulkheads (Cole-Parmer EW-45508-30) cut at the barbed end and secured with locking nuts (Cole-Parmer EW-45508-30). To add structural support for the much more flexible gel a stent was designed in Fusion360 (Figure 6A). The stent was printed and parylene coated with the same materials and methods previously described and sterilized with 100% ethanol. The PDMS mixture was prepared as previously described and poured around the square steel stock (McMaster-Carr 6527K174) in the polystyrene box with bulkheads and locking nuts in place to form the PDMS box liner. After curing at 80°C for 1 hour the box liner, bulkheads and locking nuts were autoclaved for use. A 10% Redox-Cad gel solution was dissolved in prewarmed neurobasal or UltraPure water and bath sonicated at 37 °C for 30 minutes to dissolve and degas. After adding 10% (w/v) solution of mTG (1.5:100 μL gel), 5 mL of gel solution was poured into the 22 × 22 mm PDMS box fully assembled with silicon tubing and support stent

inserted. The system was incubated and allowed to crosslink overnight. The PDMS-lined polystyrene box was perfused with the fluorescent tau^{P301L} PBS solution for 60 minutes. Instead of extracting small pieces using a 1mm biopsy punch as described by O'Grady et al. (2019), the gel was briefly frozen at -20°C to prepare for slicing and carefully sectioned into 16 even slices using a sharp, single edge razor blade. Since the chamber is only 4.5 mm, only the first 4 slices were relevant for analysis. The gel slices were incubated in a 24-well plate at 37°C in a 2%(w/v) collagenase type IV (Thermofisher 17104019) in UltraPure water solution for 1 hour. Once dissolved, samples were filtered in Amicon Ultra-2 Centrifugal Units, first using 50K molecular weight cutoffs (Sigma Aldrich, cat. No. UFC205024) followed by 30K (UFC 203024) to separate the maximum collagenase (68-130 kDa) and 300 bloom gelatin (50-100 kDa) in solution before recovering the 30 kDa retentate of focus (tau^{P301L} MW 46,920 Da). Calibration standards and extracted liquid were measured using a microplate reader (Cytation3 image reader, BioTek, Winooski, VT) with ex/em settings 540/579, gain 100. An area of non-perfused hydrogel was sampled and dissolved prior to perfusion for background subtraction of residual collagenase/gel components that were not filtered. Concentrations with error are obtained after processing fluorescence by normalizing the background subtracted readings, reported as the average and standard deviation of three independent experiments.

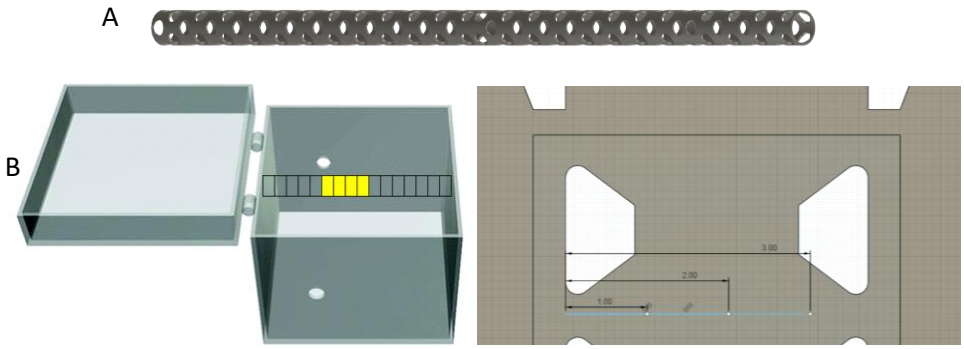

Figure 6: (A) Simple 3D printed stent used to support gel around the 1/16" diameter channel formation (top). (B) Open-box diffusion system (left) modified from O'Grady et al. (2019)[49,55] to validate simulation output in the microdevice channel (right) by extracting concentrations from discrete slices at relevant distances (mm) to the gel/reservoir interface.

2.10 | Cell viability analysis

The membrane-permeable live-cell labeling dye Calcein, AM (UltraPure grade 148504-34-1, AAT Bioquest, 22003) was added to media at 1 μM concentration from 1 mM stock in DMSO (Sigma D2650). Propidium iodide (Sigma P4864) was added at 1:1000 dilution from the 1 mg/mL water solution. After adding both dyes to media, the cells were incubated for 1.5 hours before replacing media and imaging using a Zeiss LSM 710 confocal microscope (Zeiss Microscopy, Munich, Germany). The neurons were assayed between days 14-30 after embedding. Live/dead analysis was achieved by collecting 16 stacked images along the gel depth and tiled to capture the entire length of the cell chamber. The resulting image stacks were quantified using free, open-source ImageJ software (Fiji[56], National Institutes of Health, Bethesda, MD, USA), first by processing to reduce background and creating a Z-Projection of max intensity for both channels. The signals were binarized and segmented using the Watershed function to better separate clusters into individual cells for counting. Finally, signals were quantified with the Analyze Particles macro with inclusion criteria minimum of 5 to reduce noise inclusion. Reported live percentages with error represent the average and standard deviations, respectively of at least three independent experiments.

2.11| Fixation, staining and quantification of cell-laden gels

At 7 days post diffusion experiment as described in section 2.6, cells were fixed with 4% paraformaldehyde in PBS (Thermo Scientific J19943K2) for 2 minutes and rinsed 3× and washed 10× for 20 min each with PBS. Cells were blocked and permeabilized using a buffer solution of 10% goat serum (Thermo Scientific 50062Z) in PBS (1:1) with 0.03% triton X-100 left overnight at 4°C. Primary antibody Phospho-tau (Thermo Scientific MN1020) was added at 1:50 dilution in buffer rocking overnight at 4°C, then washed the next day with PBS at least 10× 20 min each. Either secondary donkey anti-Mouse-488 or donkey anti-Mouse-555 (Thermo Scientific A-21202/A-31570) were added at 2μg/mL (1:1000 dilution) incubated overnight at 4°C rocking. The next day cells were washed at least 10× for 20 min each with PBS, anti-beta III Tubulin antibody (abcam ab190575) was added in buffer at 1:500 dilution overnight. After washing the next day at least 10× for 20 min each with PBS, 0.25% Thioflavin T in UltraPure (ThT SC-359849A, Santa Cruz Biotechnologies) was added for 30 min and washed 3× ethanol:PBS (30:70) for 5 min and 10× with PBS for 20 min. Finally, cells were counterstained with DAPI (1:5000 in PBS, Thermo Scientific D1306) for at least 15 min and imaged under a Zeiss LSM 710 confocal microscope using 10×,

20× and 40× objectives. Each laser was collected separately, with Fluor 488, 555 and 647 excited using the 488, 514 and 633 laser lines with detection at (511-630 nm), (545-697 nm), and (638-755 nm) respectively. Thioflavin T (ThT) binds oligomers and larger aggregates and undergoes a dramatic enhancement in quantum yield and shift in fluorescence upon binding, potentially due to inhibition of free rotation of its constituent aromatic rings[57]. Its excitation can range from 437-458 when bound and was captured using the 458 laser with detection at 470–496 nm. DAPI was excited using the 405 laser with emission detected at 410-465 nm.

Images were quantified to compare phosphorylated-tau signal intensity in neurites, between control (N = 2) and treated conditions (N = 3). Prior to measurement a background area distinct from discernible signal was measured from the raw image. To reduce noise and ensure average background intensities were < 1, the image brightness/contrast was adjusted as needed. DAPI signal was processed for nuclear segmentation and dilated 3-4X so that the reported average nuclei area (expected neural diameter range between 3-18 μm[58]) would expand to cover typical soma area (expected neural diameter range of 10-25 μm[59]). The expanded nuclei areas were overlayed to the Phospho-tau signal and regions were cleared to measure average remaining signal or neurite intensity. Individual background measurements were subtracted from the neurite intensities for final reported value. Summary of quantification results and sample immunofluorescent images can be found in the Appendix.

2.12| Flow cytometry to assess cellular uptake of fluorescently modified tau

Endocytosis of labeled tau^{P301L} was assessed by flow cytometry. Plated, iPSC-derived neurons were cultured for 100 days as described in section 2.1 and treated overnight with PBS only or 100 nM Cy3-labled tau^{P301L} protein. Cells were rinsed with PBS, incubated with Accutase and centrifuged as described above. Pelleted cells were briefly iced in Fluorescent Activated Cell Sorting (FACS) buffer consisting of PBS with 5% fetal bovine serum (FBS, Gibco 26140079). Control (N = 1) and tau^{P301L} treated (N = 1) cells were analyzed using a CellStream Flow Cytometer (Amnis, Seattle, WA) with excitation/emission 532/583. A summary of the two-stage gating strategy used and resultant plots can be found in the Appendix.

Chapter 3

Results and Discussion

3. 1| N-cadherin conjugated gelatin-based scaffold sustains neural cultures long-term

The approach detailed above aims to address challenges in studying neurological diseases, more specifically tauopathies. The objective of this work is to promote tau seeding activity and examine the outcome in a 3D synaptically connected neural network; thus, the first step was validating successful synthesis of the matrix essential to sustaining live neural networks for extended periods.

Synthesized Redox-Cad gel should contain key peaks around 2.5-2.8 ppm (Figure 7) from methine hydrogens on the tertiary and secondary carbons respectively, suggesting presence of valine residues which are not present in gelatin. Additionally, faint peaks at 7 ppm are indicative of the aromatic hydrogens on HPA and peaks between 2.5-3 ppm are from two acrylic (2H) bonded to the carbons in-between the carboxylic acid and aromatic ring. Peaks corresponding to both structures suggest successful conjugation of both HPA and importantly N-cadherin. The ^{1}H-NMR spectrum of unmodified gelatin base can be found in the Appendix.

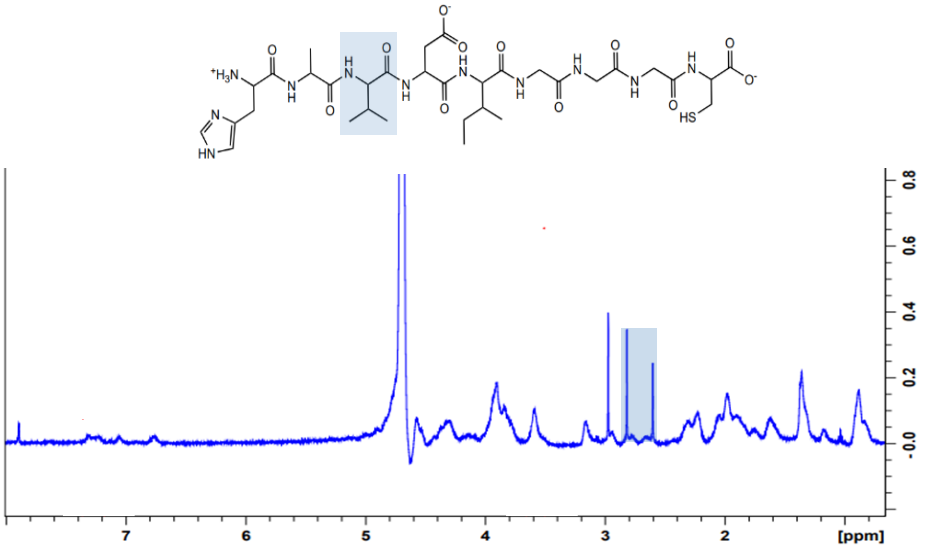

Figure 7: ^{1}H-NMR of Redox-Cad Gel with doublet peaks highlighted at ~2.5-2.8 correspond to the valine residue present on the custom N-cadherin peptide (bottom).

Furthermore, successful synthesis and conjugation of Redox-Cad is reinforced by Calcein, AM staining of embedded neurons (Figure 8). Mature iPSC-derived glutamatergic neurons demonstrated prolonged survival in Redox-Cad hydrogel in the microchannel. After more than 2-weeks post embedding, cells demonstrate neurite outgrowth and reformed synaptic connections with success comparable to the long-term viability, maturity and connectivity enhanced by similar biofunctionalized gelatin-based hydrogel GelMA-Cad[42].

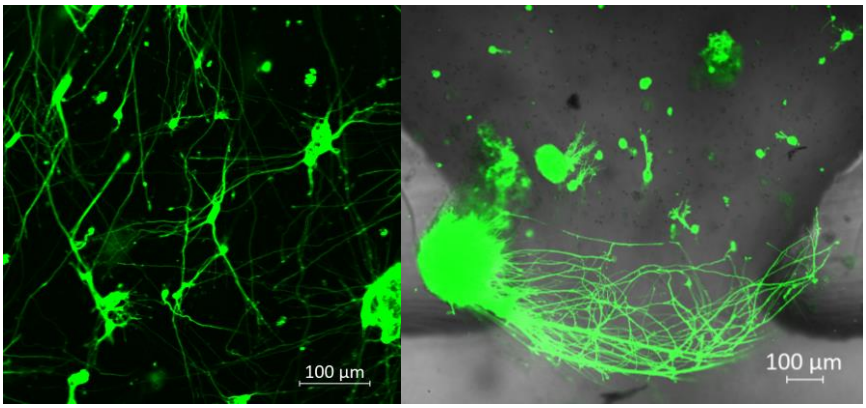

Figure 8: Viability of neurons embedded in Redox-Cad Gel after at least 14 days assayed by Calcein, AM labeling. Redox-Cad embedded neurons reform synaptic connections throughout the microdevice channel.

3. 2| Cell scaffold properties

Porosity is a key property for characterizing a cell scaffold, especially for mass transport considerations. Using the described saturation/weighing method an average porosity of 77.4 ± 9.1% (N = 4) was obtained (Table 1). Generally, high porosity is desirable to permit optimal diffusion of protein signaling and nutrient exchange. A high degree of porosity is expected and beneficial for sustaining cells long-term by supporting

oxygen/nutrient exchange and removal of waste products from the matrix[60]. Crosslinking content as well as degree of substitution may affect the porosity, pore size, and swelling behavior among other things which impact the cell microenvironment[60]. Importantly, these properties affect cell seeding efficiency and diffusion which are important considerations in transport analysis.

Porosity (%)
70.71
83.13
68.62
87.19

Table 1: Porosity measurements (N=4) determined using a variation of the Archimedes/gravimetric weighing method.

In further characterization of the cell scaffold structure and morphology, SEM images were quantified to compare properties of cell-laden and acellular hydrogels. Surface porosity by SEM analysis was calculated to be only 49.9 ± 2.5%; however, this is using 2-dimensional analysis to estimate volume of three-dimensional spaces therefore lower values than physical measurement is anticipated. A comparison between acellular and cell-laden gels showed maintained properties in terms of porous structures. Crosslinked hydrogels of both samples displayed submicron sized pores (Figure 9A) as well as large, macroporous structures (Figure 9B). The macroporous structures in cell-laden gels may appear slightly larger attributed to remodeling of the hydrogel matrix.

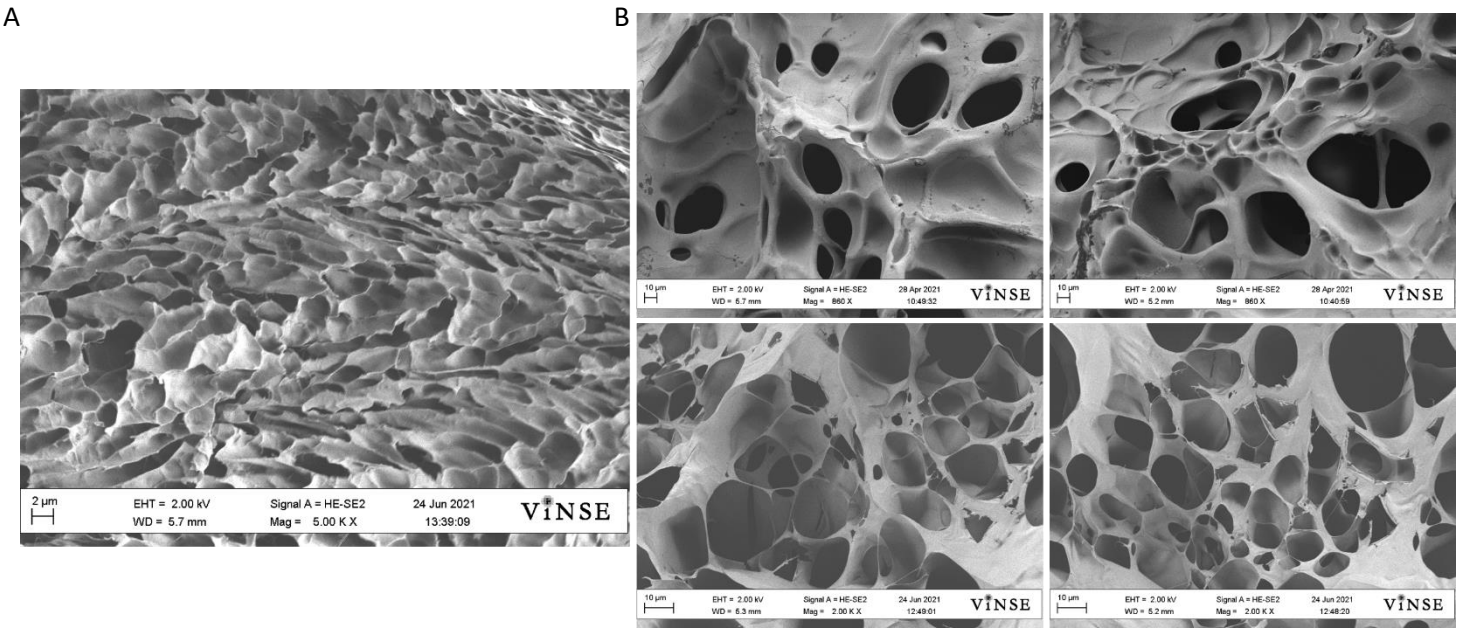

Figure 9: SEM image of dried, crosslinked hydrogel showing submicron sized pores (A) and large, macroporous structures (B) in both acellular (bottom) and samples containing neurons (top). Images were processed for quantifying pore area in ImageJ.

3. 3| COMSOL simulation and validation

In attempt to achieve an exposure gradient to promote seeding activity and propagation, diffusion was used to gradually deliver tau to allow neurons to internalize. Modeling was used to understand the rate and spatial concentration of monomer available for internalization throughout the microdevice channel. The duration of treatment was chosen based on the developed COMSOL simulation with the input parameters described above. The simulation enabled prediction of the 3-hour concentration profile after delivering 300 nM of labeled tau^{P301L} by charging the left reservoir. According to prediction, the neurons at the edge of the gel interface (x = 0) would receive the near maximum dose of tau, while those at the center received a much smaller dose (50-150 nM) and those at the opposite end (x = 4.5 mm) received minimal (< 10 nM) to no dose at the conclusion of the diffusion experiment. After 3 hours, the protein source was removed by flushing until equilibrium concentration is reached (Figure 10).

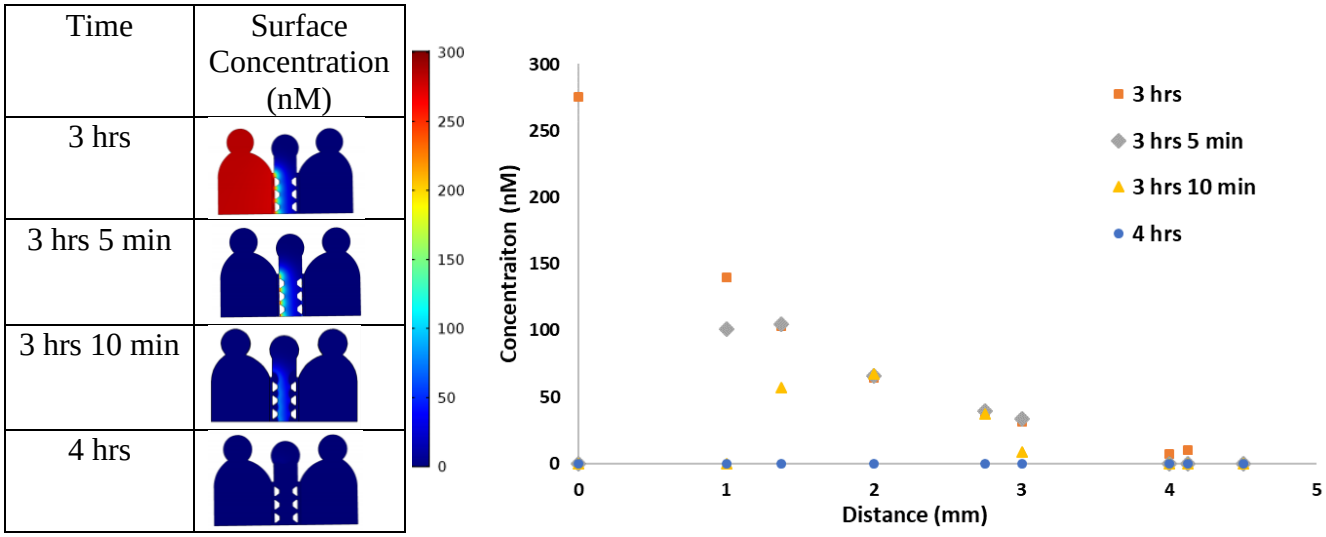

Figure 10: Visualization of COMSOL output after the left source was charged with 300 nM protein (red) and allowed to diffuse for 3 hours (left), after which, the media was flushed and gradually reached equilibrium with negligible concentration remaining in the gel by 4 hours (right).

This model was validated in a simpler geometry compared to 60 minutes of diffusion (summarized in Figure 11). The experimentally determined concentrations were slightly higher than COMSOL prediction at all sample points, which could be a result of several challenges in this method. First, the high background as a result of imperfect filtering and background subtraction is evident by the relatively large standard error. Also, there is inevitable inaccuracy in manually slicing the gel in increments slightly greater than 1 mm (~1.4 mm) that encompass a range and do not perfectly reflect the exact distances reported by COMSOL. Regardless of these difficulties, the general trend is clear and supports the COMSOL prediction.

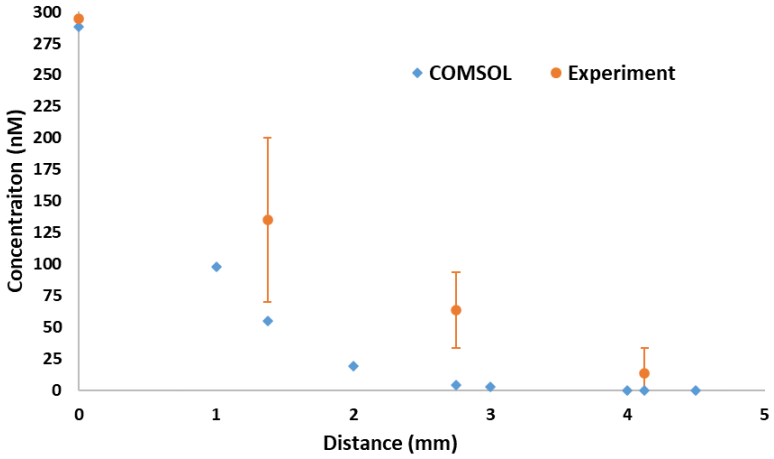

Figure 11: Comparison between COMSOL prediction and concentration determined by fluorescent extraction experiment.

3. 4| Live/dead analysis

After 7 days incubation with the mutant monomer, cells were assayed to assess viability. Cell viability was analyzed by region of the microdevice to determine whether proximity to the tau gradient or media reservoirs impacted the proportion of live survival. After normalizing to control (N = 2) live count across the entire gel volume (83.0% ± 10.3), less than half the treated cells survived (N = 4, 41.1% ± 8.4 summarized in Figure 12) in most trials.

A

Live (% total volume)
35.8
37.3
35.6
55.6

Control (media + PBS) diffusion

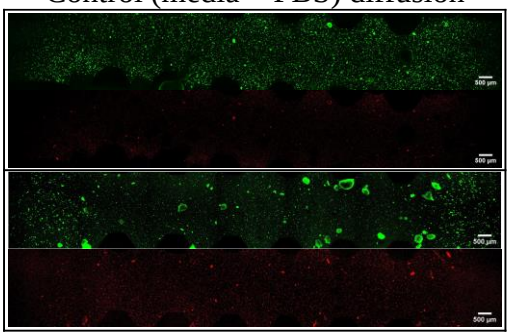

B

Tau^{P301L} diffusion

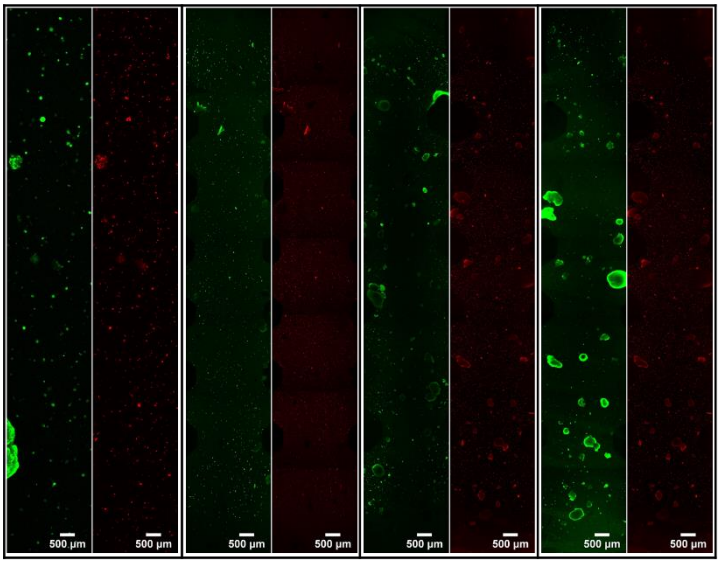

Figure 12: (A) Live/dead analysis (N=4) after normalizing to control percentage of 83.0% ± 10.3 (N = 2, compressed z-stacks below of Calcein, AM/propidium iodide-stained neurons in the microchannel 7 days after diffusion of media with PBS). (B) Compressed images of Calcein, AM/propidium iodide-stained neurons in the microchannel 7 days after diffusion of tau^{P301L}.

To determine whether survival was impacted by location within the microchannel the gel volume was divided to compare volume percentages to center, top or bottom half (closest to and furthest from the tau gradient respectively). The regional analysis in control used to normalize for analysis is provided in the Appendix. As summarized in Figure 13, there appeared to be no dependence of viability on proximity to the tau gradient. Since the gel depth did not considerably effect cell integrity, any shielding or exposure from shear stress was not significant and similarly observed in both treated and control conditions. These implications further support the propagation of pathological tau between cells and regions. Additionally, the broad range of live/dead totals among individual experiments may be due to differences in cell distribution possible during the embedding and gel setting processes (such as uniform suspension vs. formation of larger cell clusters). These may alter the matrix composition to somewhat slow or facilitate diffusion.

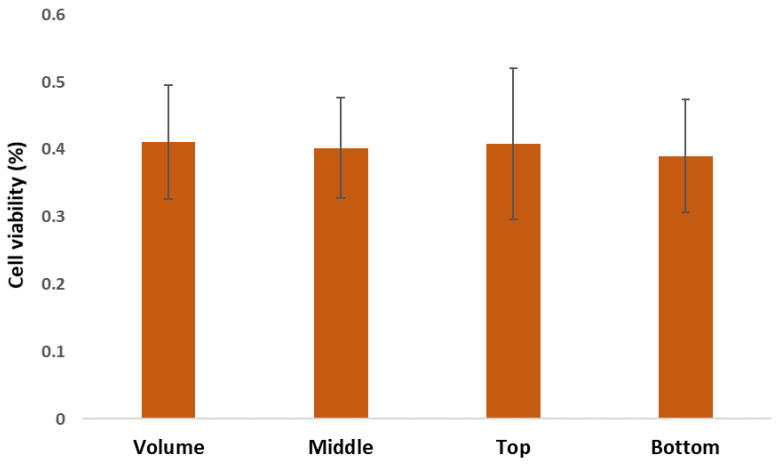

Region	Live (%)	Error
Volume	41.1	8.4
Center	36.4	7.4
Top half	38.1	11.2
Bottom half	37.7	8.4

Figure 13: Comparison of cell viability by microchannel region revealed no significant difference between the complete volume, center or portion of gel closest to (top half) or furthest from (bottom) the tau gradient.

Still, from this data it can be inferred that the mutant tau was internalized by some endocytic mechanism- through a rapid or slower pathway is uncertain from this simple assay. According to the model prediction, very little tau should remain in the gel after the gradient is diminished and equilibrium reached. With minimal residual monomer remaining in the gel after the media change it is probable the neurons internalized the mutant tau within the timeframe of the diffusion experiment and initiated nucleation/propagation to interconnected neurons resulting in the widespread pathologic effect; however, more diffusion and incubation durations would need to be investigated to confirm. Whether actively released or non-specifically once cell damage incurred is yet to be determined. If not taken up by a rapid, receptor-mediated pathway they may have entered by slower, bulk endocytosis/micropinocytosis during incubation.

Similar uptake assays of exogenous tau in two-dimensional iPSC-derived cortical cultures support this hypothesis. Microscopy and flow cytometry verified that fluorescently labeled, full-length mutant monomers (and also oligomers) are taken up from extracellular space over the course of 24 hours and occur as rapidly as 10 minutes to a few hours (1-4)[47,61,62]. Concentrations are typically on the scale of 2.5-250 nM and were efficiently internalized comparable to uptake of wild-type, and the P301S mutation did not confer the ability to aggregate during a 4-hour incubation period[61]. Labeled monomers effectively entered healthy neurons after just 10 minutes of exposure and irrespective of amine or maleimide-labeling method (the position/nature of dye was irrelevant) and detected present for at least 4 days per time-lapse imaging[61].

3. 5| Conclusions and future work

The intent of this work is to address key considerations towards the development of an iPSC-derived neural tissue model for studying tau pathology. This aim was approached by first characterizing and validating the artificial cellular microenvironment. Next, a predictive simulation of the system was created to understand diffusion of a disease-relevant, aggregation-prone mutant of tau, and finally we studied the physical model to evaluate cell viability. Toxicity of extracellular tau^{P301L} monomer was analyzed by live/dead staining to determine if the dose rate and gradient produced an observable effect. The amount of fluorescently labeled tau diffused in just 3 hours produced a dramatic response in iPSC-derived neurons after 7 days of incubation, suggesting the neurons actively internalized the monomer and initiated a

pathologic response, potentially aggregation induced neural dysfunction. At the conclusion of the incubation period roughly half the cells remained viable for further kinetic/live assays, other disease-relevant outcomes or even testing efficacy of therapeutic intervention.

Although this model is in early phases of development, preliminary data supports the materials used for generating synaptically connected neural networks capable of reproducing aspects of neurodegeneration. These are important steps in developing a 3D in vitro neuronal model for studying mechanisms of tau pathogenesis. Several outcomes intended to be addressed in future iterations include whether neural networks exposed to comparable concentrations of various tau, such as mutant or pre-aggregated forms, produce an equivalent response. Additional time points may be examined, and more comprehensive uptake assays and metrics for cell damage will be performed such as flow cytometry, western blot analysis and immunofluorescence staining. To potentially isolate more specific receptors/carrier molecules involved in this rapid endocytosis of monomeric form and potentially larger aggregates specific anti-tau antibodies or CRISPR/Cas9 genomic engineering may be considered [63].

Disease models may be used to help elucidate mechanisms for therapeutic improvements by gaining more in-depth understanding of the pathways involved, confirmations and regions of tau required for uptake. Ultimately, it is necessary to precisely map functions of neuronal release and internalization. More specifically, to distinguish healthy extracellular tau from pathogenic to pave the way for more specific inhibitors and preventative strategies to interfere with intercellular transfer of pathogenic forms without interfering with physiological processes that may rely on the transfer of healthy tau for biological function.

Appendix

Fluorescently modified tau^{P301L} was investigated in a microfluidic hydrogel system by diffusing and evaluating biological response in iPSC-derived neurons. Confocal fluorescence microscopy and immunocytochemistry (ICC) was used to assess cell viability or identify presence of tau amyloid/aggregate formations and phosphorylated tau protein in an effort to detect and quantify and qualitatively compare these markers which are prevalent in tau-mediated neurodegeneration.

Analytical characterization of hydrogel properties

I have included a stacked view of ^{1}H-NMR spectrums of unmodified gelatin base and final conjugated Redox Cad hydrogel for convenient comparison of the added peaks from the valine residue of N-cadherin.

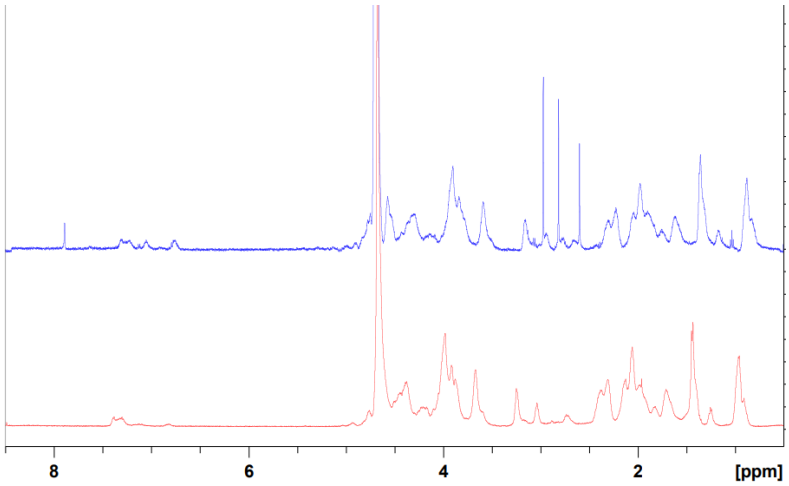

Figure A-1: ^{1}H-NMR spectrum of unmodified gelatin base (bottom) at 37 °C lack the prominent pair of peaks at ~2.5-2.8 from valine after N-cadherin conjugation in Redox Cad gel (top).

Next, I have included data used to calculate the porosity of the hydrogel using a formula based on the gravimetric method, where W_{dry} is the dry mass, W_1 is that of the 10 mL centrifuge tube filled with UltraPure water, W_2 the mass of the centrifuge tube and immersed hydrogel, and W_3 is that remaining after removing the hydrated sample. There is some variability in measurement likely due to measurement error and difficulty in fully saturating all pores in the 3D sample.

Dry Weight (mg)	W_1 (g)	W_2 (g)	W_3 (g)	Porosity (%)
24.8	**21.25**	**21.26**	**21.18**	**70.71**
28.3	**20.44**	**20.46**	**20.40**	**83.13**
25	**21.48**	**21.49**	**21.43**	**68.62**
36	**21.42**	**21.45**	**21.37**	**87.19**

Table A-1: Measured weights and calculated porosity of Redox-Cad hydrogel samples.

Measuring and predicting diffusion in porous hydrogel

Apart from porosity, another important parameter in characterizing diffusion dynamics is the effective diffusion coefficient, which was validated and estimated in multiple experiments. The increase in fluorescence of Cy5 or Cy3-labeled tau^{P301L} as the protein diffused across the microfluidic hydrogel channel was measured by fluorescence microscopy. Intensity of resulting time-lapse images was used to extract concentrations. A solution to Fick's Second law correlation was used to determine a best fitting diffusion coefficient by minimizing the mean squared error between the model output and experiment. An example of this fit is provided in Figure A-2.

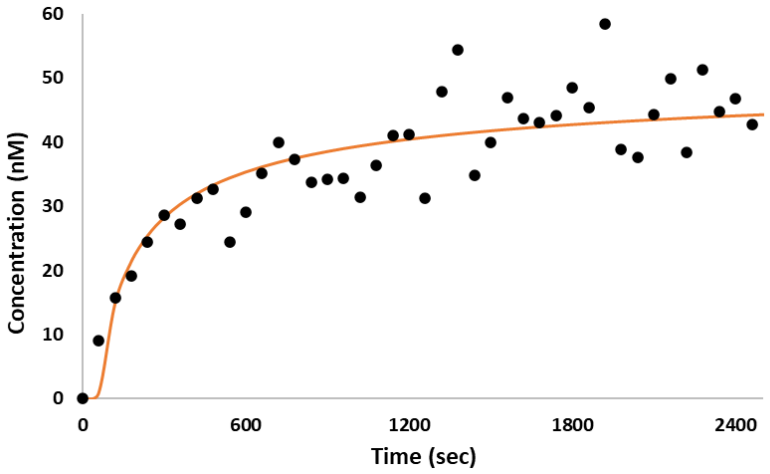

Figure A-2: Solution to Fick's Second Law with calculated effective diffusion coefficient determined from time-lapse fluorescent images.

A COMSOL model was formed and to validate simulation prediction, a physical system based on work from O'Grady et al. (2019)[49,55] was used to enable discrete sampling of the hydrogel after a timed diffusion experiment. The liquid was extracted by dissolving and molecular weight filtering and measured by a microplate reader which allowed sensitive detection of the low protein concentrations and fluid volume. The fluorescent intensity was collected at known concentrations to create a calibration standard (Table A-2, ex/em settings 540/579, gain 100) and a linear regression relationship (Figure A-3) correlated measured intensity obtained from hydrogel in validation experiments to protein concentration.

Concentration	**300 nM**	**250 nM**	**200 nM**	**150 nM**	**100 nM**	**50 nM**	**45 nM**	**0 nM**
	4446	3257	2737	2085	1368	755	331	8
	4403	3655	2031	1638	1102	716	295	9
	4531	3929	3293	1889	1293	696	664	6
Average	**4460.0**	**3613.7**	**2687.0**	**1870.7**	**1254.3**	**722.3**	**430.0**	**7.7**

Table A-2: Calibration standards of Cy3-labeled tau^{P301L}.

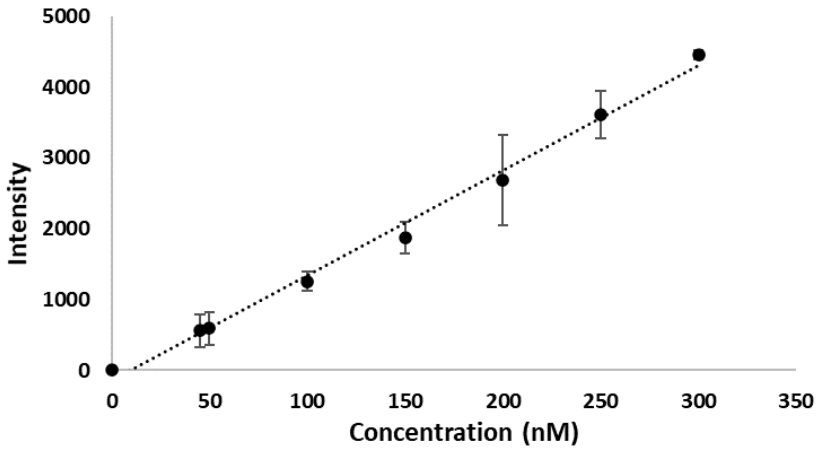

Figure A-3: Calibration standards of Cy3-labeled tau^{P301L}.

End-point assays for confirming uptake and indication of tau-induced dysfunction

The toxicity of fluorescently labeled tau^{P301L} assessed by cell viability assay 7 days after the 3-hour diffusion revealed distinction between response of tau^{P301L} treated cells and those that received only PBS in media. The treated conditions did not significantly vary in cell health by region (Figure 13) and the control conditions did not likewise (Table A-3) suggesting shear stress imparted from media changes or laser exposure during experiment did not discriminately impact cell integrity.

Region	Live (%)	Error
Volume	83.0	10.3
Center	86.2	14.1
Top half	86.0	10.5
Bottom half	82.7	17.0

Table A-3: Cell viability as a percentage assessed by Calcein-AM/Propidium Iodide stain and quantification, 7-days after control diffusion experiment averaged separately in four regions of the microdevice channel.

Confocal fluorescence microscopy was performed after immunostaining cells to analyze extent of phosphorylated tau in the system. Examples of immunofluorescent images of tau^{P301L} treated (Figure A-4) and control cells (Figure A-5) of iPSC-derived neurons fixed in hydrogel 7 days after diffusion experiment is provided below. Qualitatively comparing the phosphorylated tau (Phospho-tau, Thermo Scientific MN1020) signal intensity and morphology, the tau^{P301L} treated cells appear to have significantly greater puncta structures possibly deposits, as well as linear patterns stretching from nuclei (DAPI) identifying branching neurites.

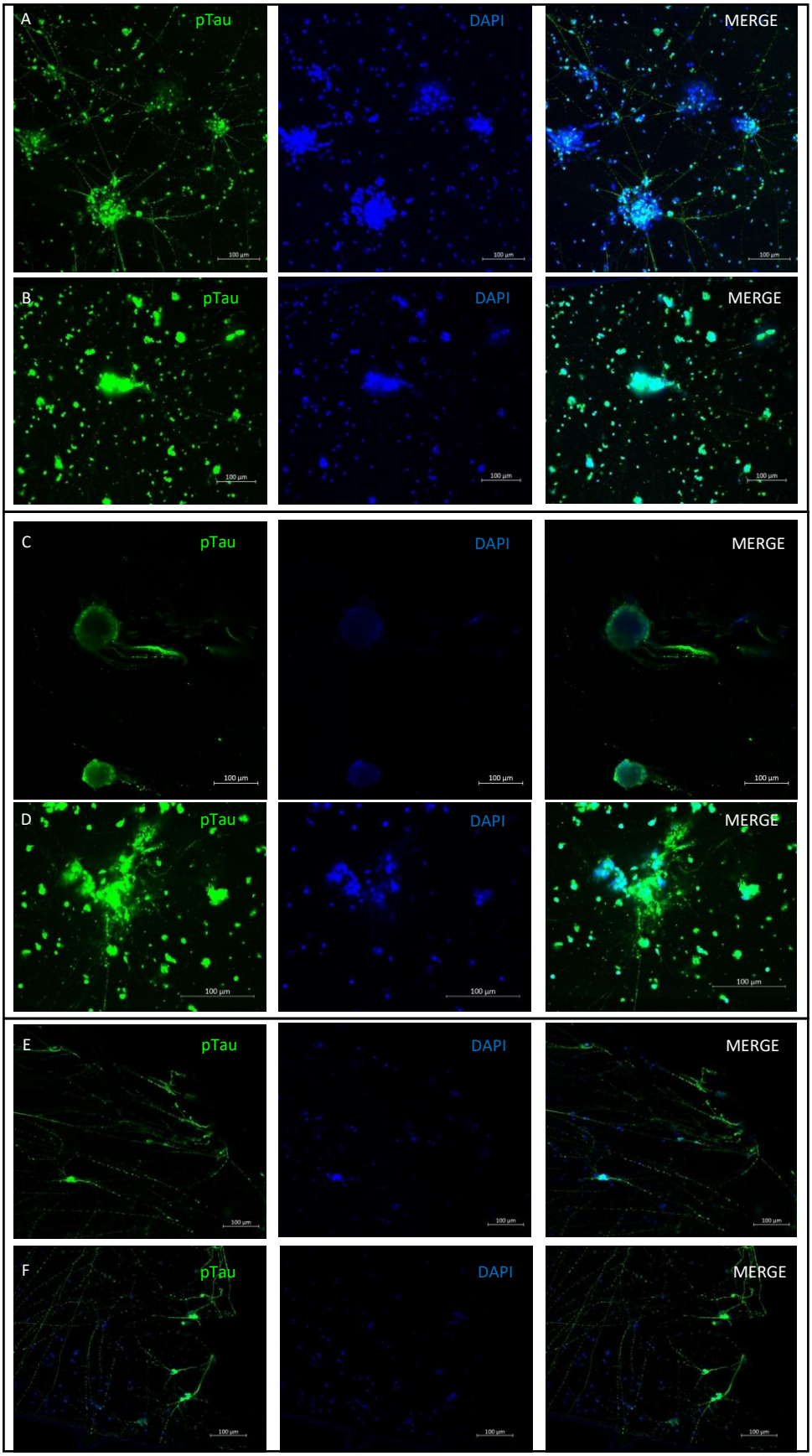
tauP301L treated
Left edge
A
pTau
DAPI
MERGE
B
pTau
DAPI
MERGE
tauP301L treated
Middle
C
pTau
DAPI
MERGE
D
pTau
DAPI
MERGE
tauP301L treated
Right edge
E
pTau
DAPI
MERGE
F
pTau
DAPI
MERGE

Figure A-4: Immunocytochemistry of tauP301L treated cells fixed on day 7 after diffusion, sorted and labeled by proximity to gel/reservoir interface and in decreasing order of tau exposure.

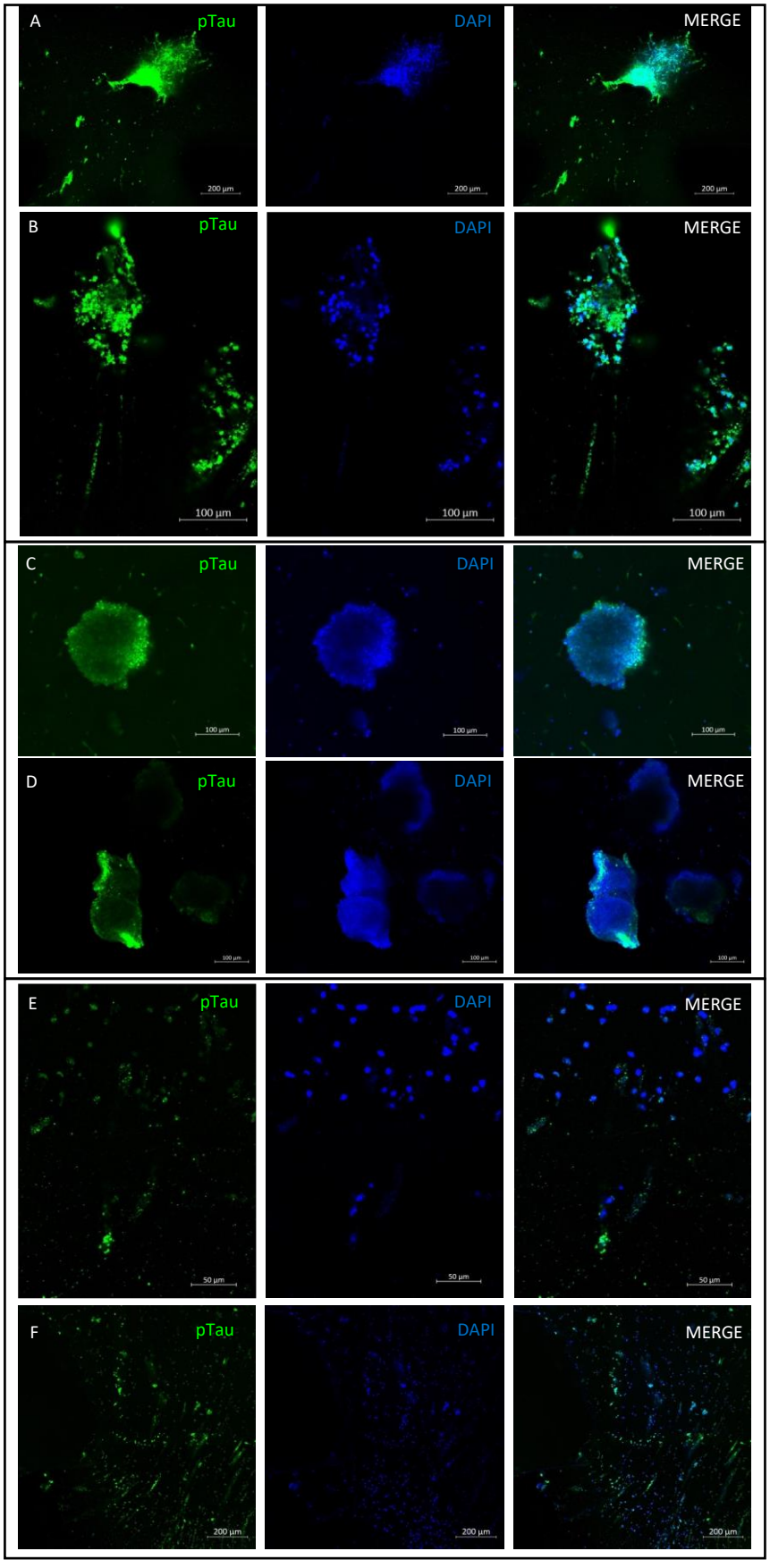
A
pTau
DAPI
MERGE
Control
Left edge
B
pTau
DAPI
MERGE
100 µm
C
pTau
DAPI
MERGE
Control
Middle
D
pTau
DAPI
MERGE
E
pTau
DAPI
MERGE
Control
Right edge
F
pTau
DAPI
MERGE

Figure A-5: ICC of control cells fixed 7 days after diffusion experiment, sorted and labeled by proximity to gel/reservoir interface.

Further analysis of phosphorylated tau (pTau) signal intensity associated with neurites was performed using ImageJ by separately measuring intensity outside expanded nuclei (DAPI) regions after processing and subtracting individual background measurements (Figure A-6). Average background values for control and treated groups were within standard error of each other suggesting observed differences in signal intensity between groups was not a result of background and noise. Statistical analysis was performed in GraphPad software (Prism, San Diego, CA) for assessment with Welch's t-test for an associated p-value of 0.0097 (<0.05 significant). The high degree of variability indicates additional samples would be beneficial to increase statistical power and improve comparison in future studies.

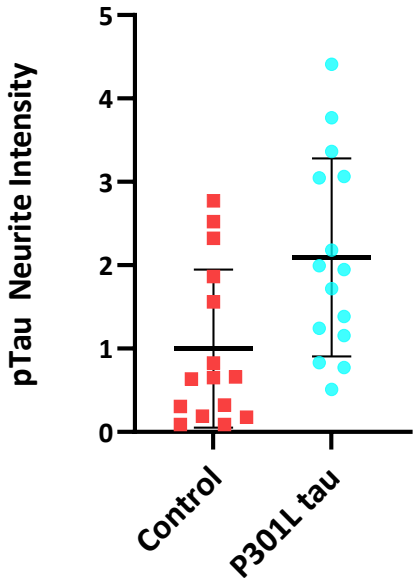

Figure A-6: Average phospho-tau (pTau) signal intensity quantified in neurites for treated (N = 3) and control (N = 2) conditions normalized to the average control measurement Each data point represents the average pTau neurite intensity selected and measured from the image collection of control or P301L tau experiments.

Flow cytometry assay was used to analyze two-dimensional cellular uptake of Cy3-labeled tau^{P301L} in plated iPSC-derived neurons treated for 24 hours. Data were processed using two-stage gating with first level on forward/side scatter (FSC/SSC) density plots to exclude debris in the bottom left and identify the cell population, followed by gating on aspect ratio (0.6 – 1.0) for doublet discrimination (Figure A-7, left). Out of singlets, greater than 3000 cells were analyzed for each sample and as shown in the histogram (Figure A-7, right), the treated cells (P301L Tau-Cy3, N = 1) exhibited increased luminescence intensity, suggesting internalization whereas PBS treated cells (Control, N = 1) displayed some background but very few with high luminescence, however more analysis is required to determine extent fluorescence associated with membrane-bound or completely internalized, intracellular protein.

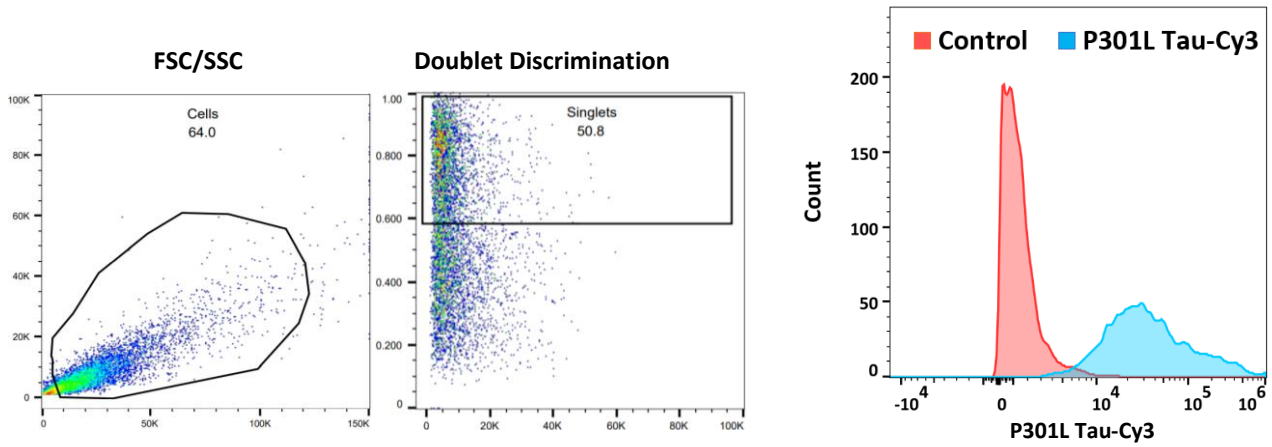

Figure A-7: Uptake of Cy3-labeled tauP301L by flow cytometry analysis, showing the two-stage gating strategy (left) and resulting histogram of cell count against luminescent intensity.

REFERENCES

(1) Wray, S. Modelling Neurodegenerative Disease Using Brain Organoids. *Semin. Cell Dev. Biol.* **2020**, S1084952119300011. https://doi.org/10.1016/j.semcdb.2020.05.012.

(2) Grenier, K.; Kao, J.; Diamandis, P. Three-Dimensional Modeling of Human Neurodegeneration: Brain Organoids Coming of Age. *Mol. Psychiatry* **2020**, *25* (2), 254–274. https://doi.org/10.1038/s41380-019-0500-7.

(3) Centeno, E. G. Z.; Cimarosti, H.; Bithell, A. 2D versus 3D Human Induced Pluripotent Stem Cell-Derived Cultures for Neurodegenerative Disease Modelling. *Mol. Neurodegener.* **2018**, *13* (1), 27. https://doi.org/10.1186/s13024-018-0258-4.

(4) Guzman-Martinez, L.; Maccioni, R. B.; Andrade, V.; Navarrete, L. P.; Pastor, M. G.; Ramos-Escobar, N. Neuroinflammation as a Common Feature of Neurodegenerative Disorders. *Front. Pharmacol.* **2019**, *10*. https://doi.org/10.3389/fphar.2019.01008.

(5) García-León, J. A.; Cabrera-Socorro, A.; Eggermont, K.; Swijsen, A.; Terryn, J.; Fazal, R.; Nami, F.; Ordovás, L.; Quiles, A.; Lluis, F.; Serneels, L.; Wierda, K.; Sierksma, A.; Kreir, M.; Pestana, F.; Van Damme, P.; De Strooper, B.; Thorrez, L.; Ebneth, A.; Verfaillie, C. M. Generation of a Human Induced Pluripotent Stem Cell-Based Model for Tauopathies Combining Three Microtubule-Associated Protein TAU Mutations Which Displays Several Phenotypes Linked to Neurodegeneration. *Alzheimers Dement. J. Alzheimers Assoc.* **2018**, *14* (10), 1261–1280. https://doi.org/10.1016/j.jalz.2018.05.007.

(6) Reilly, P.; Winston, C. N.; Baron, K. R.; Trejo, M.; Rockenstein, E. M.; Akers, J. C.; Kfoury, N.; Diamond, M.; Masliah, E.; Rissman, R. A.; Yuan, S. H. Novel Human Neuronal Tau Model Exhibiting Neurofibrillary Tangles and Transcellular Propagation. *Neurobiol. Dis.* **2017**, *106*, 222–234. https://doi.org/10.1016/j.nbd.2017.06.005.

(7) Strang, K. H.; Croft, C. L.; Sorrentino, Z. A.; Chakrabarty, P.; Golde, T. E.; Giasson, B. I. Distinct Differences in Prion-like Seeding and Aggregation between Tau Protein Variants Provide Mechanistic Insights into Tauopathies. *J. Biol. Chem.* **2018**, *293* (7), 2408–2421. https://doi.org/10.1074/jbc.M117.815357.

(8) Hefti, M. M.; Farrell, K.; Kim, S.; Bowles, K. R.; Fowkes, M. E.; Raj, T.; Crary, J. F. High-Resolution Temporal and Regional Mapping of MAPT Expression and Splicing in Human Brain Development. *PLOS ONE* **2018**, *13* (4), e0195771. https://doi.org/10.1371/journal.pone.0195771.

(9) Tau-441, (2N4R), P301L mutant | rPeptide https://www.rpeptide.com/products/proteins/tau/t-1014-1 (accessed 2021 -05 -19).

(10) MAPT S320F | ALZFORUM https://www.alzforum.org/mutations/mapt-s320f (accessed 2020 -12 -04).

(11) Strang, K. H.; Golde, T. E.; Giasson, B. I. MAPT Mutations, Tauopathy, and Mechanisms of Neurodegeneration. *Lab. Invest.* **2019**, *99* (7), 912–928. https://doi.org/10.1038/s41374-019-0197-x.

(12) MAPT P301S | ALZFORUM https://www.alzforum.org/mutations/mapt-p301s (accessed 2020 -08 -08).

(13) MAPT P301L | ALZFORUM https://www.alzforum.org/mutations/mapt-p301l (accessed 2020 -08 -11).

(14) Dawson, H. N.; Cantillana, V.; Chen, L.; Vitek, M. P. The Tau N279K Exon 10 Splicing Mutation Recapitulates Frontotemporal Dementia and Parkinsonism Linked to Chromosome 17 Tauopathy in a Mouse Model. *J. Neurosci.* **2007**, *27* (34), 9155–9168. https://doi.org/10.1523/JNEUROSCI.5492-06.2007.

(15) Meraz-Rios, M.; Lira-De León, K. I.; Campos-Peña, V.; De Anda, M.; Mena-López, R. Tau Oligomers and Aggregation in Alzheimer's Disease. *J. Neurochem.* **2009**, *112*, 1353–1367. https://doi.org/10.1111/j.1471-4159.2009.06511.x.

(16) Iqbal, K.; Liu, F.; Gong, C.-X.; Grundke-Iqbal, I. Tau in Alzheimer Disease and Related Tauopathies. *Curr. Alzheimer Res.* **2010**, *7* (8), 656–664.

(17) Lim, S.; Haque, Md. M.; Kim, D.; Kim, D. J.; Kim, Y. K. Cell-Based Models To Investigate Tau Aggregation. *Comput. Struct. Biotechnol. J.* **2014**, *12* (20), 7–13. https://doi.org/10.1016/j.csbj.2014.09.011.

(18) Vogel, J. W.; Young, A. L.; Oxtoby, N. P.; Smith, R.; Ossenkoppele, R.; Strandberg, O. T.; La Joie, R.; Aksman, L. M.; Grothe, M. J.; Iturria-Medina, Y.; Pontecorvo, M. J.; Devous, M. D.; Rabinovici, G. D.; Alexander, D. C.; Lyoo, C. H.; Evans, A. C.; Hansson, O. Four Distinct Trajectories of Tau Deposition Identified in Alzheimer's Disease. *Nat. Med.* **2021**, *27* (5), 871–881. https://doi.org/10.1038/s41591-021-01309-6.

(19) Brunello, C. A.; Merezhko, M.; Uronen, R.-L.; Huttunen, H. J. Mechanisms of Secretion and Spreading of Pathological Tau Protein. *Cell. Mol. Life Sci.* **2020**, *77* (9), 1721–1744. https://doi.org/10.1007/s00018-019-03349-1.

(20) Takeda, S. Tau Propagation as a Diagnostic and Therapeutic Target for Dementia: Potentials and Unanswered Questions. *Front. Neurosci.* **2019**, *13*. https://doi.org/10.3389/fnins.2019.01274.

(21) Mudher, A.; Colin, M.; Dujardin, S.; Medina, M.; Dewachter, I.; Naini, S. M. A.; Mandelkow, E.-M.; Mandelkow, E.; Buée, L.; Goedert, M.; Brion, J.-P. What Is the Evidence That Tau Pathology Spreads through Prion-like Propagation? *Acta Neuropathol. Commun.* **2017**, *5*. https://doi.org/10.1186/s40478-017-0488-7.

(22) Holmes, B. B.; DeVos, S. L.; Kfoury, N.; Li, M.; Jacks, R.; Yanamandra, K.; Ouidja, M. O.; Brodsky, F. M.; Marasa, J.; Bagchi, D. P.; Kotzbauer, P. T.; Miller, T. M.; Papy-Garcia, D.; Diamond, M. I. Heparan Sulfate Proteoglycans Mediate Internalization and Propagation of Specific

Proteopathic Seeds. *Proc. Natl. Acad. Sci.* **2013**, *110* (33), E3138–E3147. https://doi.org/10.1073/pnas.1301440110.

(23) Kaniyappan, S.; Tepper, K.; Biernat, J.; Chandupatla, R. R.; Hübschmann, S.; Irsen, S.; Bicher, S.; Klatt, C.; Mandelkow, E.-M.; Mandelkow, E. FRET-Based Tau Seeding Assay Does Not Represent Prion-like Templated Assembly of Tau Filaments. *Mol. Neurodegener.* **2020**, *15*. https://doi.org/10.1186/s13024-020-00389-1.

(24) Vogels, T.; Leuzy, A.; Cicognola, C.; Ashton, N. J.; Smolek, T.; Novak, M.; Blennow, K.; Zetterberg, H.; Hromadka, T.; Zilka, N.; Schöll, M. Propagation of Tau Pathology: Integrating Insights From Postmortem and In Vivo Studies. *Biol. Psychiatry* **2020**, *87* (9), 808–818. https://doi.org/10.1016/j.biopsych.2019.09.019.

(25) Puangmalai, N.; Bhatt, N.; Montalbano, M.; Sengupta, U.; Gaikwad, S.; Ventura, F.; McAllen, S.; Ellsworth, A.; Garcia, S.; Kayed, R. Internalization Mechanisms of Brain-Derived Tau Oligomers from Patients with Alzheimer's Disease, Progressive Supranuclear Palsy and Dementia with Lewy Bodies. *Cell Death Dis.* **2020**, *11* (5), 1–16. https://doi.org/10.1038/s41419-020-2503-3.

(26) Slanzi, A.; Iannoto, G.; Rossi, B.; Zenaro, E.; Constantin, G. In Vitro Models of Neurodegenerative Diseases. *Front. Cell Dev. Biol.* **2020**, *8*. https://doi.org/10.3389/fcell.2020.00328.

(27) Caneus, J.; Akanda, N.; Rumsey, J. W.; Guo, X.; Jackson, M.; Long, C. J.; Sommerhage, F.; Georgieva, S.; Kanaan, N. M.; Morgan, D.; Hickman, J. J. A Human Induced Pluripotent Stem Cell-derived Cortical Neuron Human-on-a Chip System to Study Aβ42 and Tau-induced Pathophysiological Effects on Long-term Potentiation. *Alzheimers Dement. Transl. Res. Clin. Interv.* **2020**, *6* (1). https://doi.org/10.1002/trc2.12029.

(28) Li, L.; Chao, J.; Shi, Y. Modeling Neurological Diseases Using IPSC-Derived Neural Cells. *Cell Tissue Res.* **2018**, *371* (1), 143–151. https://doi.org/10.1007/s00441-017-2713-x.

(29) Yeung, J. H. Y.; Palpagama, T. H.; Tate, W. P.; Peppercorn, K.; Waldvogel, H. J.; Faull, R. L. M.; Kwakowsky, A. The Acute Effects of Amyloid-Beta1–42 on Glutamatergic Receptor and Transporter Expression in the Mouse Hippocampus. *Front. Neurosci.* **2020**, *13*. https://doi.org/10.3389/fnins.2019.01427.

(30) Liu, J.; Chang, L.; Song, Y.; Li, H.; Wu, Y. The Role of NMDA Receptors in Alzheimer's Disease. *Front. Neurosci.* **2019**, *13*. https://doi.org/10.3389/fnins.2019.00043.

(31) Yap, M. S.; Nathan, K. R.; Yeo, Y.; Lim, L. W.; Poh, C. L.; Richards, M.; Lim, W. L.; Othman, I.; Heng, B. C. Neural Differentiation of Human Pluripotent Stem Cells for Nontherapeutic Applications: Toxicology, Pharmacology, and In Vitro Disease Modeling https://www.hindawi.com/journals/sci/2015/105172/ (accessed 2020 -08 -10). https://doi.org/10.1155/2015/105172.

(32) Jorfi, M.; D'Avanzo, C.; Kim, D. Y.; Irimia, D. Three-Dimensional Models of the Human Brain Development and Diseases. *Adv. Healthc. Mater.* **2018**, *7* (1). https://doi.org/10.1002/adhm.201700723.

(33) Yi, Y.; Park, J.; Lim, J.; Lee, C. J.; Lee, S.-H. Central Nervous System and Its Disease Models on a Chip. *Trends Biotechnol.* **2015**, *33* (12), 762–776. https://doi.org/10.1016/j.tibtech.2015.09.007.

(34) Hernández Vera, R.; O'Callaghan, P.; Fatsis-Kavalopoulos, N.; Kreuger, J. Modular Microfluidic Systems Cast from 3D-Printed Molds for Imaging Leukocyte Adherence to Differentially Treated Endothelial Cultures. *Sci. Rep.* **2019**, *9* (1), 11321. https://doi.org/10.1038/s41598-019-47475-z.

(35) de Almeida Monteiro Melo Ferraz, M.; Nagashima, J. B.; Venzac, B.; Le Gac, S.; Songsasen, N. 3D Printed Mold Leachates in PDMS Microfluidic Devices. *Sci. Rep.* **2020**, *10* (1), 994. https://doi.org/10.1038/s41598-020-57816-y.

(36) Walsh, D. I.; Kong, D. S.; Murthy, S. K.; Carr, P. A. Enabling Microfluidics: From Clean Rooms to Makerspaces. *Trends Biotechnol.* **2017**, *35* (5), 383–392. https://doi.org/10.1016/j.tibtech.2017.01.001.

(37) Anguiano, M.; Castilla, C.; Maška, M.; Ederra, C.; Peláez, R.; Morales, X.; Muñoz-Arrieta, G.; Mujika, M.; Kozubek, M.; Muñoz-Barrutia, A.; Rouzaut, A.; Arana, S.; Garcia-Aznar, J. M.; Ortiz-de-Solorzano, C. Characterization of Three-Dimensional Cancer Cell Migration in Mixed Collagen-Matrigel Scaffolds Using Microfluidics and Image Analysis. *PLOS ONE* **2017**, *12* (2), e0171417. https://doi.org/10.1371/journal.pone.0171417.

(38) Chen, G.; Gulbranson, D. R.; Hou, Z.; Bolin, J. M.; Ruotti, V.; Probasco, M. D.; Smuga-Otto, K.; Howden, S. E.; Diol, N. R.; Propson, N. E.; Wagner, R.; Lee, G. O.; Antosiewicz-Bourget, J.; Teng, J. M. C.; Thomson, J. A. Chemically Defined Conditions for Human IPS Cell Derivation and Culture. *Nat. Methods* **2011**, *8* (5), 424–429. https://doi.org/10.1038/nmeth.1593.

(39) Coating Plates with Matrigel® for Pluripotent Stem Cell Culture https://www.stemcell.com/coating-plates-with-matrigel-for-pluripotent-stem-cell-culture.html (accessed 2020 -08 -10).

(40) Lippmann, E. S.; Estevez-Silva, M. C.; Ashton, R. S. Defined Human Pluripotent Stem Cell Culture Enables Highly Efficient Neuroepithelium Derivation Without Small Molecule Inhibitors. *STEM CELLS* **2014**, *32* (4), 1032–1042. https://doi.org/10.1002/stem.1622.

(41) Shi, Y.; Kirwan, P.; Livesey, F. J. Directed Differentiation of Human Pluripotent Stem Cells to Cerebral Cortex Neurons and Neural Networks. *Nat. Protoc.* **2012**, *7* (10), 1836–1846. https://doi.org/10.1038/nprot.2012.116.

(42) O'Grady, B. J.; Balotin, K. M.; Bosworth, A. M.; McClatchey, P. M.; Weinstein, R. M.; Gupta, M.; Poole, K. S.; Bellan, L. M.; Lippmann, E. S. Development of an N-Cadherin Biofunctionalized Hydrogel to Support the Formation of Synaptically Connected Neural Networks. *ACS Biomater. Sci. Eng.* **2020**, *6* (10), 5811–5822. https://doi.org/10.1021/acsbiomaterials.0c00885.

(43) Chambers, S. M.; Fasano, C. A.; Papapetrou, E. P.; Tomishima, M.; Sadelain, M.; Studer, L. Highly Efficient Neural Conversion of Human ES and IPS Cells by Dual Inhibition of SMAD Signaling. *Nat. Biotechnol.* **2009**, *27* (3), 275–280. https://doi.org/10.1038/nbt.1529.

(44) PDMS Bonding https://harrickplasma.com/pdms-bonding/ (accessed 2021 -06 -16).

(45) Song, X.; Zhu, C.; Fan, D.; Mi, Y.; Li, X.; Fu, R. Z.; Duan, Z.; Wang, Y.; Feng, R. R. A Novel Human-Like Collagen Hydrogel Scaffold with Porous Structure and Sponge-Like Properties. *Polymers* **2017**, *9* (12). https://doi.org/10.3390/polym9120638.

(46) NHS ester labeling of amino biomolecules https://www.lumiprobe.com/protocols/nhs-ester-labeling (accessed 2021 -03 -24).

(47) Usenovic, M.; Niroomand, S.; Drolet, R. E.; Yao, L.; Gaspar, R. C.; Hatcher, N. G.; Schachter, J.; Renger, J. J.; Parmentier-Batteur, S. Internalized Tau Oligomers Cause Neurodegeneration by Inducing Accumulation of Pathogenic Tau in Human Neurons Derived from Induced Pluripotent Stem Cells. *J. Neurosci.* **2015**, *35* (42), 14234–14250. https://doi.org/10.1523/JNEUROSCI.1523-15.2015.

(48) Mass Balance Equation for Transport of Diluted Species in Porous Media https://doc.comsol.com/5.6/doc/com.comsol.help.corr/corr_ug_chemsptrans.08.108.html#2035525 (accessed 2021 -05 -22).

(49) O'Grady, B.; Balikov, D. A.; Wang, J. X.; Neal, E. K.; Ou, Y.-C.; Bardhan, R.; Lippmann, E. S.; Bellan, L. M. Spatiotemporal Control and Modeling of Morphogen Delivery to Induce Gradient Patterning of Stem Cell Differentiation Using Fluidic Channels. *Biomater. Sci.* **2019**, *7* (4), 1358–1371. https://doi.org/10.1039/C8BM01199K.

(50) *COMSOL Multiphysics® v. 5.2a. Www.Comsol.Com. COMSOL AB, Stockholm, Sweden*.

(51) Poon, C. *Measuring the Density and Viscosity of Culture Media for Optimized Computational Fluid Dynamics Analysis of in Vitro Devices*; 2020. https://doi.org/10.1101/2020.08.25.266221.

(52) Toonkool, P.; Regan, D. G.; Kuchel, P. W.; Morris, M. B.; Weiss, A. S. Thermodynamic and Hydrodynamic Properties of Human Tropoelastin: ANALYTICAL ULTRACENTRIFUGE AND PULSED FIELD-GRADIENT SPIN-ECHO NMR STUDIES *. *J. Biol. Chem.* **2001**, *276* (30), 28042–28050. https://doi.org/10.1074/jbc.M103391200.

(53) Flach, K.; Hilbrich, I.; Schiffmann, A.; Gärtner, U.; Krüger, M.; Leonhardt, M.; Waschipky, H.; Wick, L.; Arendt, T.; Holzer, M. Tau Oligomers Impair Artificial Membrane Integrity and Cellular Viability. *J. Biol. Chem.* **2012**, *287* (52), 43223–43233. https://doi.org/10.1074/jbc.M112.396176.

(54) COMSOL Multiphysics Reference Manual. 1622.

(55) O'Grady, B. J.; Balikov, D. A.; Lippmann, E. S.; Bellan, L. M. Spatiotemporal Control of Morphogen Delivery to Pattern Stem Cell Differentiation in Three-Dimensional Hydrogels. *Curr. Protoc. Stem Cell Biol.* **2019**, *51* (1), e97. https://doi.org/10.1002/cpsc.97.

(56) Schindelin, J.; Arganda-Carreras, I.; Frise, E.; Kaynig, V.; Longair, M.; Pietzsch, T.; Preibisch, S.; Rueden, C.; Saalfeld, S.; Schmid, B.; Tinevez, J.-Y.; White, D. J.; Hartenstein, V.; Eliceiri, K.; Tomancak, P.; Cardona, A. Fiji: An Open-Source Platform for Biological-Image Analysis. *Nat. Methods* **2012**, *9* (7), 676–682. https://doi.org/10.1038/nmeth.2019.

(57) Shen, D.; Coleman, J.; Chan, E.; Nicholson, T. P.; Dai, L.; Sheppard, P. W.; Patton, W. F. Novel Cell- and Tissue-Based Assays for Detecting Misfolded and Aggregated Protein Accumulation Within Aggresomes and Inclusion Bodies. *Cell Biochem. Biophys.* **2011**, *60* (3), 173–185. https://doi.org/10.1007/s12013-010-9138-4.

(58) Organization of Cell Types (Section 1, Chapter 8) Neuroscience Online: An Electronic Textbook for the Neurosciences | Department of Neurobiology and Anatomy - The University of Texas Medical School at Houston https://nba.uth.tmc.edu/neuroscience/m/s1/chapter08.html (accessed 2021 -07 -15).

(59) Gilman, J. P.; Medalla, M.; Luebke, J. I. Area-Specific Features of Pyramidal Neurons—a Comparative Study in Mouse and Rhesus Monkey. *Cereb. Cortex* **2017**, *27* (3), 2078–2094. https://doi.org/10.1093/cercor/bhw062.

(60) Sun, M.; Sun, X.; Wang, Z.; Guo, S.; Yu, G.; Yang, H. Synthesis and Properties of Gelatin Methacryloyl (GelMA) Hydrogels and Their Recent Applications in Load-Bearing Tissue. *Polymers* **2018**, *10* (11). https://doi.org/10.3390/polym10111290.

(61) Evans, L. D.; Wassmer, T.; Fraser, G.; Smith, J.; Perkinton, M.; Billinton, A.; Livesey, F. J. Extracellular Monomeric and Aggregated Tau Efficiently Enter Human Neurons through Overlapping but Distinct Pathways. *Cell Rep.* **2018**, *22* (13), 3612–3624. https://doi.org/10.1016/j.celrep.2018.03.021.

(62) Rauch, J. N.; Luna, G.; Guzman, E.; Audouard, M.; Challis, C.; Sibih, Y. E.; Leshuk, C.; Hernandez, I.; Wegmann, S.; Hyman, B. T.; Gradinaru, V.; Kampmann, M.; Kosik, K. S. LRP1 Is a Master Regulator of Tau Uptake and Spread. *Nature* **2020**, *580* (7803), 381–385. https://doi.org/10.1038/s41586-020-2156-5.

(63) Silva, M. C.; Cheng, C.; Mair, W.; Almeida, S.; Fong, H.; Biswas, M. H. U.; Zhang, Z.; Huang, Y.; Temple, S.; Coppola, G.; Geschwind, D. H.; Karydas, A.; Miller, B. L.; Kosik, K. S.; Gao, F.-B.; Steen, J. A.; Haggarty, S. J. Human IPSC-Derived Neuronal Model of Tau-A152T Frontotemporal Dementia Reveals Tau-Mediated Mechanisms of Neuronal Vulnerability. *Stem Cell Rep.* **2016**, *7* (3), 325–340. https://doi.org/10.1016/j.stemcr.2016.08.001.